remote sensing

MDPI

Article

Discriminating Seagrasses from Green Macroalgae in European Intertidal Areas Using High-Resolution Multispectral Drone Imagery

Simon Oiry [1], Bede Ffinian Rowe Davies [1], Ana I. Sousa [2], Philippe Rosa [1], Maria Laura Zoffoli [3], Guillaume Brunier [4], Pierre Gernez [1] and Laurent Barillé [1,*]

[1] Institut des Substances et Organismes de la Mer, ISOMer, Nantes Université, UR 2160, F-44000 Nantes, France; simon.oiry@univ-nantes.fr
[2] ECOMARE, CESAM—Centre for Environmental and Marine Studies, Department of Biology, University of Aveiro, Campus Universitário de Santiago, 3810-193 Aveiro, Portugal
[3] Consiglio Nazionale delle Ricerche, Istituto di Scienze Marine (CNR-ISMAR), 00133 Rome, Italy
[4] BRGM French Geological Survey, Cayenne 97300, French Guiana
* Correspondence: laurent.barille@univ-nantes.fr

Abstract: Coastal areas support seagrass meadows, which offer crucial ecosystem services, including erosion control and carbon sequestration. However, these areas are increasingly impacted by human activities, leading to habitat fragmentation and seagrass decline. In situ surveys, traditionally performed to monitor these ecosystems, face limitations on temporal and spatial coverage, particularly in intertidal zones, prompting the addition of satellite data within monitoring programs. Yet, satellite remote sensing can be limited by too coarse spatial and/or spectral resolutions, making it difficult to discriminate seagrass from other macrophytes in highly heterogeneous meadows. Drone (unmanned aerial vehicle—UAV) images at a very high spatial resolution offer a promising solution to address challenges related to spatial heterogeneity and the intrapixel mixture. This study focuses on using drone acquisitions with a ten spectral band sensor similar to that onboard Sentinel-2 for mapping intertidal macrophytes at low tide (i.e., during a period of emersion) and effectively discriminating between seagrass and green macroalgae. Nine drone flights were conducted at two different altitudes (12 m and 120 m) across heterogeneous intertidal European habitats in France and Portugal, providing multispectral reflectance observation at very high spatial resolution (8 mm and 80 mm, respectively). Taking advantage of their extremely high spatial resolution, the low altitude flights were used to train a Neural Network classifier to discriminate five taxonomic classes of intertidal vegetation: Magnoliopsida (Seagrass), Chlorophyceae (Green macroalgae), Phaeophyceae (Brown algae), Rhodophyceae (Red macroalgae), and benthic Bacillariophyceae (Benthic diatoms), and validated using concomitant field measurements. Classification of drone imagery resulted in an overall accuracy of 94% across all sites and images, covering a total area of 467,000 m^2. The model exhibited an accuracy of 96.4% in identifying seagrass. In particular, seagrass and green algae can be discriminated. The very high spatial resolution of the drone data made it possible to assess the influence of spatial resolution on the classification outputs, showing a limited loss in seagrass detection up to about 10 m. Altogether, our findings suggest that the MultiSpectral Instrument (MSI) onboard Sentinel-2 offers a relevant trade-off between its spatial and spectral resolution, thus offering promising perspectives for satellite remote sensing of intertidal biodiversity over larger scales.

Keywords: unmaned aerial vehicule; remote sensing; coastal ecosystems; neural network; marine macrophytes

Citation: Oiry, S.; Davies, B.F.R.; Sousa, A.I.; Rosa, P.; Zoffoli, M.L.; Brunier, G.; Gernez, P.; Barillé, L. Discriminating Seagrasses from Green Macroalgae in European Intertidal Areas Using High-Resolution Multispectral Drone Imagery. *Remote Sens.* **2024**, *16*, 4383. https://doi.org/10.3390/rs16234383

Academic Editor: Javier Marcello

Received: 14 October 2024
Revised: 16 November 2024
Accepted: 20 November 2024
Published: 23 November 2024

1. Introduction

Coastal areas are vital hotspots for marine biodiversity, with intertidal seagrass meadows playing a crucial role at the interface between land and ocean [1]. Seagrass meadows

provide a myriad of ecosystem services, including carbon sequestration, oxygen production, protection against sea-level rise and coastline erosion, and mitigation of eutrophication [1,2]. They serve as vital habitats for a diverse array of marine and terrestrial species, providing living, breeding, and feeding grounds [3–5]. Due to the concentration of human activities in coastal zones, seagrass meadows are directly exposed to and impacted by anthropogenic pressures. Global regression and fragmentation of seagrass meadows are currently observed due to climate change, diseases, urbanization, land reclamation, dredging, competition with alien species, and reduction in water quality [2,6–12]. Both habitat fragmentation and reduction, in turn, can severely compromise the effectiveness of ecosystem services provided by seagrass meadows. While improvements in water quality and hydrodynamics have been recently reported in Europe, allowing an overall recovery of seagrass ecosystems at local and European scales, many coastal waters worldwide are still subjected to strong eutrophication processes [2,13,14]. Coastal eutrophication has been associated with excessive accumulation of green macroalgae (algal blooms) and so-called green tides [15]. Green tides produce shade and suffocation over seagrass individuals, thus threatening the health of seagrass ecosystems [16].

The importance of seagrass meadows and the variety of ecosystem services they provide have led to the enhancement of both global and regional programs to monitor Essential Oceanic Variable (EOVs) such as seagrass composition [17], as well as Essential Biodiversity Variable (EBVs) such as seagrass taxonomic diversity, species distribution, population abundance, and phenology [18]. Traditionally, indicators of seagrass status have been quantified using in situ measurements. However, the acquisition of field measurements in intertidal zones is notoriously challenging. Intertidal seagrass meadows are only exposed during low tide and can be situated in difficult-to-reach mudflats, potentially leading to inaccurate and limited estimations with conventional sampling techniques [19]. Satellite observations have been proven effective in complementing in situ sampling, allowing for near real-time and consistent retrieval of seagrass EOVs and EBVs over extensive meadows [14,20–24].

While satellite remote sensing (RS) provides temporally consistent observations over large spatial scales, its utilization over intertidal areas is limited by several constraints. Satellite missions with a high temporal resolution (e.g., daily MODIS observation) are limited by too coarse spatial resolution (>100 m) to accurately map patchy seagrass meadows. Missions with a high spatial resolution, such as Sentinel-2 (10 m) or Landsat 8/9 (30 m), can be limited by low spectral resolution. The limited number of spectral bands challenges the accurate discrimination of seagrass from other co-existing macrophytes such as Chlorophyceae (green algae) and marine Magnoliopsida (seagrass), which share the same pigment composition [25,26], resulting in a similar reflectance signature, especially in the visible range [27,28]. Recently, using advanced machine-learning algorithms trained with a large hyperspectral library of more than 300 field reflectance spectra, Davies et al. (2023) [28] demonstrated that it was possible to discriminate Magnoliopsida from Chlorophyceae using reflectance spectra at Sentinel-2's spectral resolution. However, the application of this approach to satellite RS remains to be validated. Moreover, patches of green algae can develop at small spatial scales that are not observable using Sentinel-2 and/or Landsat 8/9 images [29], especially during the initial stage of a green tide.

Drones (Unmanned Aerial Vehicles—UAVs) can potentially fill the data gaps left by satellite RS and in situ measurements due to their ability to provide spatially explicit observations at very high spatial resolutions (pixel size from mm to cm) while capturing data at multispectral resolutions [30,31]. The versatility of drones allows for their application across a diverse thematic range, from coastal zone monitoring and management [32–36] to mapping species distribution [2,37–41]. However, when applied to coastal habitat mapping, previous case studies were mostly limited to a low number of drone flights over a single study site, restricting the generalizability of their application over wider geographical scales [37,40,42,43]. These studies have demonstrated the capability of drones to map intertidal (and subtidal) habitats, including seagrasses; however, a broader generalization of these findings is still lacking. The current paper uniquely expands the spatial and method-

ological scope of drone-based remote sensing for intertidal habitat mapping across a broad biogeographical range. It demonstrates the feasibility of accurately classifying diverse macrophyte types across various study sites, with a particular focus on distinguishing Magnoliopsida (seagrasses) and Chlorophyceae (green algae). Unlike previous studies, our approach integrates multiple spatial scales by simulating satellite resolutions and quantifying the impact of spatial resolution on classification accuracy. Nine drone flights were performed over soft-bottom (mud and sand) intertidal areas along the Atlantic coastlines of two European countries (France and Portugal), covering a wide range of habitats, from monospecific seagrass meadows to meadows mixed with green or red macroalgae.

A deep learning algorithm was trained and validated for macrophyte discrimination, emphasizing applicability across diverse sites without losing prediction accuracy. The classification maps obtained at a very high spatial resolution with the drone were spatially degraded to satellite resolutions, making it possible to assess the effect of spatial resolution on classification accuracy and provide insights for coastal habitat mapping using satellite remote sensing. This study is, therefore, among the first to quantify the effects of spatial resolution on the accuracy of drone-based intertidal macrophyte classification across a wide geographical scale, providing a framework to better understand satellite-based classification challenges.

2. Material & Methods

2.1. Study Sites

Seven study sites distributed between France and Portugal were selected for their extensive intertidal seagrass beds. Two sites were located in the Gulf of Morbihan, France (Figure 1A: 47.5791°N, 2.8018°W). This gulf covers an area of 115 km^2 and is only connected to the sea through a 900 m wide channel. A total of 53 small islands are scattered across the gulf, leading to 250 km of shorelines. Patchy seagrass meadows can be found on many of these islands. One of the sites within the gulf was on one of its islands (Arz), and the other was located further south on a mainland beach area (Duer). The Gulf of Morbihan is a Natura 2000 site and a Regional Protected Area due to its rich biodiversity, including its seagrass meadows, and is also classified as a RAMSAR site, which highlights its significance as a wetland of international importance. Two other sites were located in Bourgneuf Bay, France (Figure 1B: 46.9849°N, 2.1488°W), which is a 340 km^2 semi-enclosed macrotidal bay protected from waves by Noirmoutier Island. Bourgneuf Bay hosts a large intertidal seagrass meadow of about 6 km^2 [44]. Within this meadow, the sites observed by drones (L'Epine and Barbatre) contained monospecific beds of *Zostera noltei* (dwarf eelgrass) with very little mixing with other macrophytes. Bourgneuf Bay is also part of the Natura 2000 network and serves as a RAMSAR site due to its critical habitat for migratory bird species and its extensive seagrass meadows [5]. Three sites were surveyed in the Ria de Aveiro Coastal Lagoon in Portugal (Figure 1C: 40.6887°N, 8.6810°W). The extent of this lagoon is ~83 km^2 (at low tide), with many narrow channels, large salt marshes and many mudflats that uncover at low tide [45]. It is connected to the open sea through a single channel, with a tidal lag between the North and the South of the lagoon. The southernmost site (Gafanha) is a mudflat located in the Mira channel (one of the four main channels of the lagoon), whereas the two other sites (Mataduços and Marinha Lanzarote) were situated in the middle of the lagoon, with Marinha Lanzarote only accessible by boat. These Portuguese sites (at Ria de Aveiro) are characterized by more diverse intertidal vegetation, where patches of seagrass intermingle with red, brown, and green macroalgae. The Ria de Aveiro coastal lagoon, like the other study areas, is a Natura 2000 site, recognized for its rich mosaic of habitats (EU Habitats Directive) and importance for biodiversity, including migratory bird species (part of the EU Birds Directive) and intertidal vegetation (from mudflats to seagrass meadows and salt marshes).

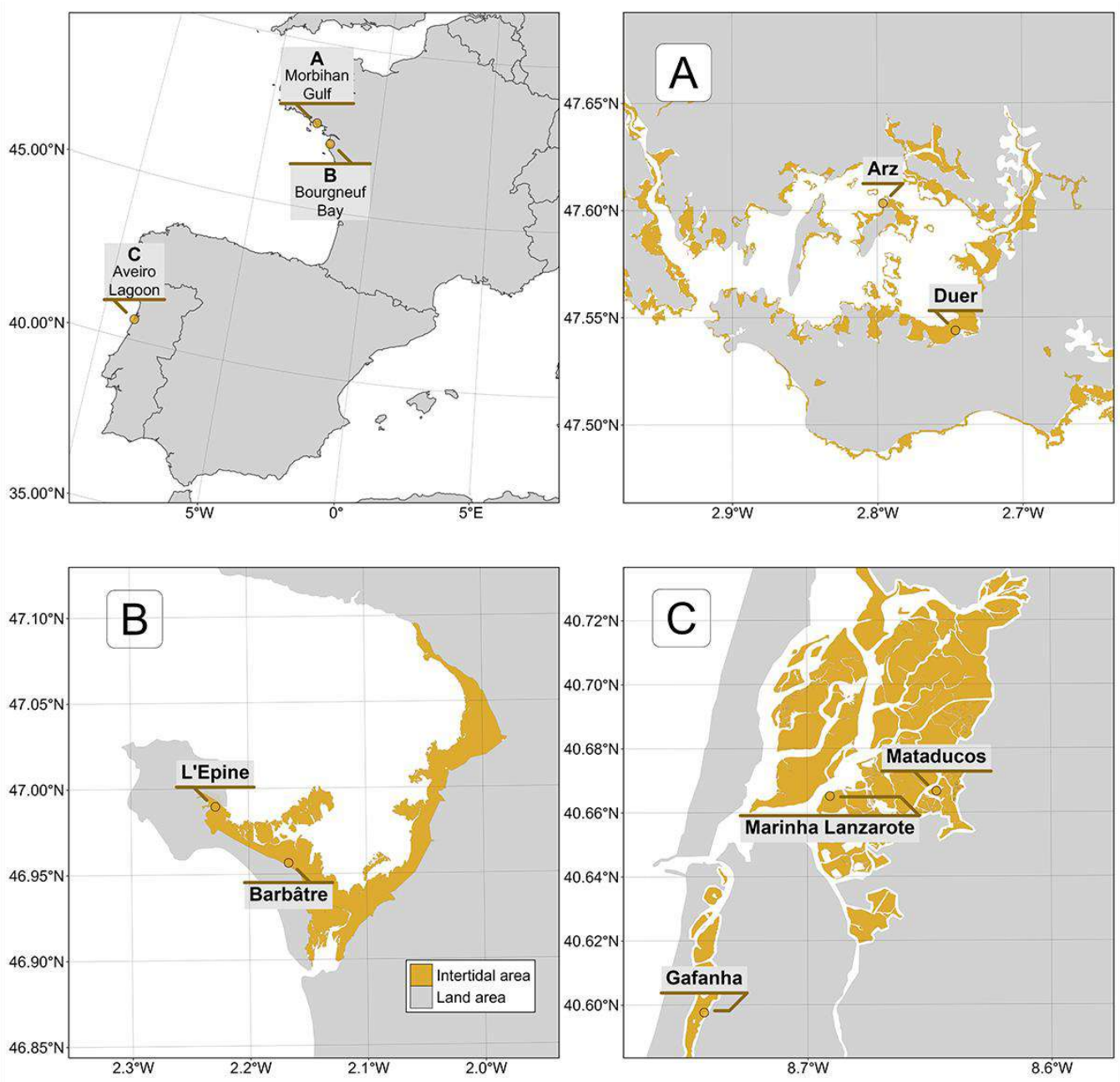

Figure 1. Location of drone flights in France and Portugal. (**A**) Gulf of Morbihan (Two sites), (**B**) Bourgneuf Bay (Two sites), and (**C**) Ria de Aveiro Coastal Lagoon (Three sites). The golden areas represent the intertidal zone.

2.2. Field Sampling

2.2.1. Drone Acquisition

At each location, a DJI Matrice 200 (DJI, Shenzhen, China) quadcopter drone equipped with a Micasense RedEdge Dual MX multispectral camera (Micasense Inc., Seattle, WA, USA) [46] was flown to take 1.2 million pixel reflectance photographs with ten spectral bands ranging from the blue to the near-infrared (NIR): 444, 475, 531, 560, 650, 668, 705, 717, 740, and 840 nm. To ensure consistent lighting conditions across flight paths, the drone's trajectory was aligned to maintain a solar azimuth angle of 90 degrees. An overlap of 70% and 80% (side and front, respectively) between each image was set for each flight. A downwelling light sensor (DLS2) was used to concomitantly acquire irradiance data with the camera measurements. Raw data were calibrated in reflectance using a calibration

panel reflective at ~50% provided by the manufacturer. Across all sites, flights were made at two different altitudes: 12 m or/and 120 m, with a spatial resolution of 8 mm and 80 mm, respectively (Table 1). Low-altitude flights, with a spatial resolution of 8 mm, were used to build the training dataset for the neural network, as this high resolution allowed for precise photo-interpretation of vegetation classes. In contrast, high-altitude flights were used for validation purposes.

Table 1. List of drone flights, summarizing the date, the altitude, and the purpose of each flight. The 12 m and 120 m flights have a spatial resolution of 8 and 80 mm, respectively.

Country	Site	Name	Altitude	Utility	Date
France	Gulf of Morbihan	Arz Island	12 m	Training	29 September 2022
		Duer	12 m	Training	14 July 2022
		Duer	120 m	Validation	14 July 2022
	Bourgneuf Bay	Barbâtre	120 m	Validation	7 September 2021
		L'Epine	120 m	Validation	8 July 2021
Portugal	Aveiro Lagoon	Marinha Lanzarote	120 m	Validation	17 June 2022
		Mataduços	120 m	Validation	16 June 2022
		Gafanha	120 m	Validation	15 June 2022
		Gafanha	12 m	Training	15 June 2022

2.2.2. Ground Control Points

Before each flight, targets used as ground control points were distributed over the study site and georeferenced with a Trimble © Geo XH 6000 differential GPS (dGPS; Trimble Inc., Westminster, CO, USA). Ground control points were used to correct georeferencing imprecision of orthomosaics with a horizontal and vertical accuracy of 10 cm. A dGPS was also used to georeferenced quadrats of 0.25 m^2, which assessed the presence or absence of five key taxonomic classes of intertidal vegetation: Bacillariophyceae (benthic diatoms forming biofilms at the sediment surface during low tide, with biofilm's size ranging from small patches (m^2) to entire mudflats (km^2); henceforth, Benthic diatoms), Phaeophyceae (brown macroalgae generally attached to rocks or other substrates able to form dense beds in the intertidal zone; henceforth, brown macroalgae), Magnoliopsida (seagrasses, rooted flowering marine plants able to form extensive meadows on soft sediments; henceforth, seagrasses), Chlorophyceae (green macroalgae, typically found attached to rocks or washed ashore; henceforth, green macroalgae), and Rhodophyceae (red macroalgae, attached to hard substrates but can also be found on soft-bottom substrate; henceforth, red macroalgae) (Figure 2). Only homogeneous vegetation patches extending over several meters were selected as ground control points. Pictures of each quadrat were uploaded online to the open-portal Global Biodiversity Information Facility (GBIF) platform [47]. Each photograph was also processed to estimate the percent cover of each type of vegetation using image processing software (ImageJ v1.46). Hyperspectral reflectance signatures of each vegetation class were recorded using an ASD FieldSpec HandHeld 2 (Malvern Panalytical, Worcestershire, UK) spectroradiometer, which acquires reflectance between 325 and 1075 nm, with 1 nm of spectral resolution. Hyperspectral signatures served dual purposes: they validated the radiometric calibration of drone data and contributed to misclassification reduction in photo interpretations.

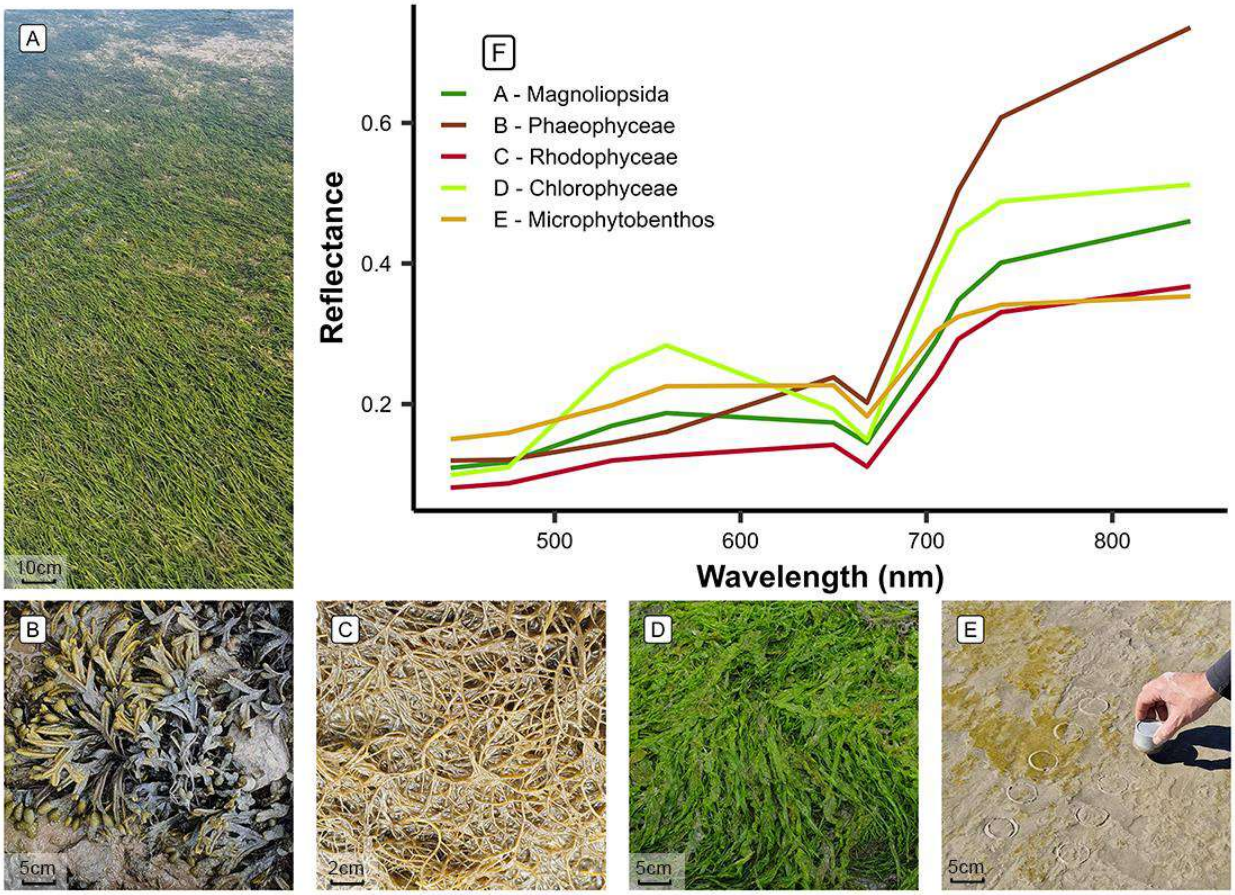

Figure 2. The five taxonomic classes of vegetation used to train the Neural Network model and an example of their raw spectral signatures at the spectral resolution of the Micasense RedEdge Dual MX. (**A**): Magnoliopsida (*Zostera noltei*); (**B**): Phaeophyceae (*Fucus* sp.); (**C**): Rhodophyceae (*Gracilaria vermiculophylla*); (**D**): Chlorophyceae (*Ulva* sp.); (**E**): Bacillariophyceae (Benthic diatoms). (**F**): Spectral signature of each vegetation class. Classes and species taxonomy following the WORMS—World Register of Marine Species classification.

2.3. Drone Processing

A structure-from-motion photogrammetry software (Agisoft Metashape v2.1.1) was used to process images to obtain multispectral ortho-mosaics of each flight. The process of ortho-mosaicking was identical for every flight. First, key tying points were detected inside each image and between overlapping images to obtain a sparse point cloud. This cloud was cleaned using a reprojection accuracy metric to remove noisy points. A dense point cloud was then produced using a structure from the motion algorithm. A surface interpolation of this dense point cloud was made to obtain a digital surface model (DSM) used to reconstruct the multispectral ortho-image [48]. Low-altitude drone flights produced ortho-images with a very high spatial resolution (8 mm per pixel), making it efficient to visually distinguish between the various types of vegetation. High-altitude flights allowed to cover larger areas and produced images with a pixel size of 80 mm (Table 1).

2.4. General Workflow

The spectral similarities of the reflectance signatures at the spectral resolution of the Micasense senor between intertidal green macrophytes (Magnoliopsida and Chlorophyceae) make their discrimination challenging using simple classification algorithms (Figure 2F). To overcome this challenge, a deep learning classification method was trained, validated, and applied to each drone flight (Figure 3).

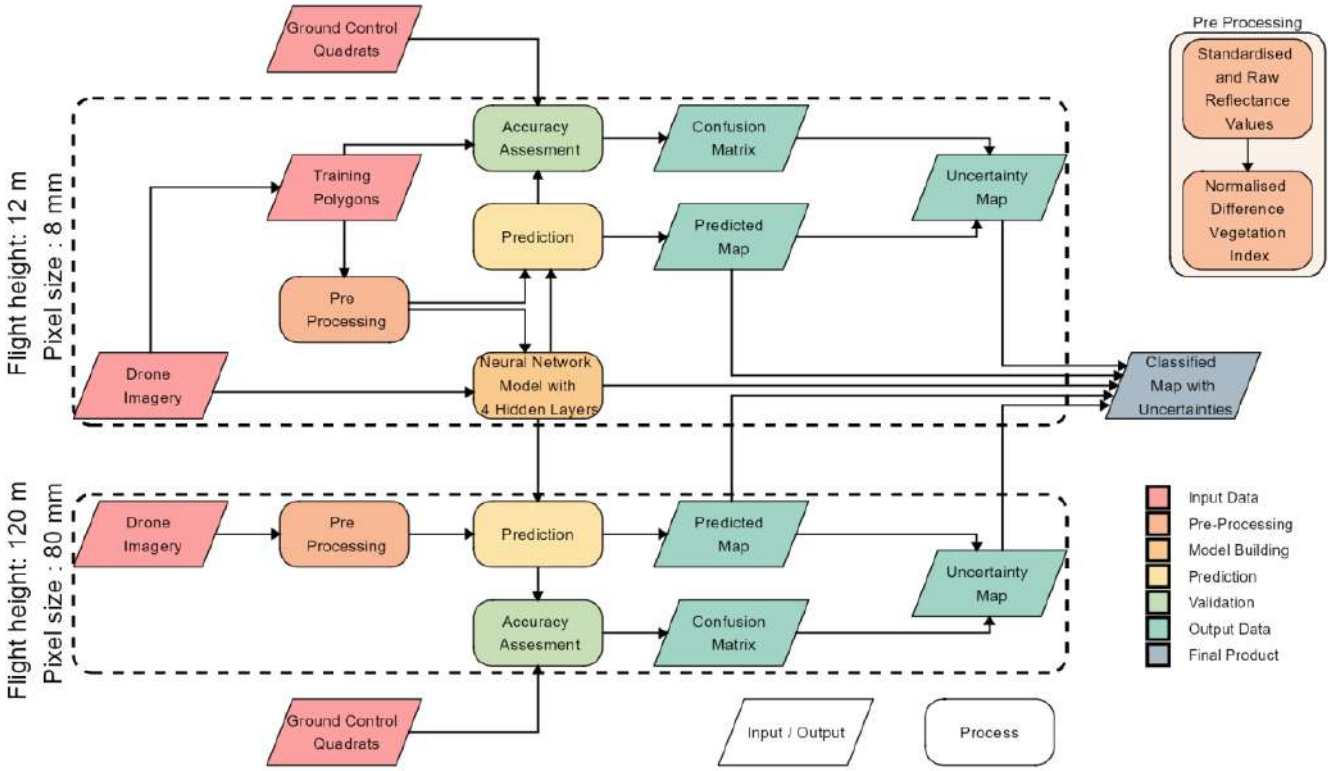

Figure 3. Schematic representation of the workflow. Parallelograms represent input or output data, and rectangles represent Python processing algorithms. The overall workflow of this study is divided into two distinct parts based on the spatial resolution of the drone flights: high-resolution flights (pixel size: 8 mm) were utilized for training and prediction of the Neural Network model, whereas lower-resolution flights (pixel size: 80 mm) were solely employed for prediction and validation purposes. Validation has been performed on both high- and low-resolution flights.

2.4.1. Training Dataset Building

A dataset containing photo-interpreted drone reflectance pixels was built to train a Neural Network model. The training pixels were categorized into seven classes, representing the habitats encountered at the different study sites: sediment, water, green macroalgae, seagrasses, benthic diatoms, brown macroalgae and red macroalgae. Only data from the low-altitude flights (Table 1) were used for training because their 8 mm spatial resolution allowed them to avoid spectral sub-pixel mixing and to accurately identify vegetation classes. In the field, seagrasses displaying two types of color were observed (i.e., whereas most seagrasses had green leaves, brownish leaves were also observed due to senescence or photo-degradation). Careful attention was given to incorporating training pixels from both color types into the training dataset for the seagrass class. This approach was consistently applied to all classes within the model. More than 418,000 pixels at 8 mm resolution from the three training flights were used to train the model (Table 2). For model training, 21 variables were used as predictors: the ten raw spectral bands of the Micasense RedEdge Dual MX multispectral camera (ranging from 444 nm to 840 nm), the same ten spectral bands standardized using a min/max transformation (Equation (1); [49]) and the Normalized Difference Vegetation Index (NDVI, Equation (2)). Standardization of spectral bands is commonly used to eliminate the scaling differences between spectra and to limit the effect of biomass on the spectra shape [25,28].

$$R_i^*(\lambda) = \frac{R_i(\lambda) - min(R_i)}{max(R_i) - min(R_i)} \quad (1)$$

where $R_i(\lambda)$ is the reflectance at the wavelength (λ) of each individual spectra (i), $min(R_i)$, and $max(R_i)$ are the minimum and maximum value of the spectra (i):

$$NDVI = \frac{R(840\text{ nm}) - R(668\text{ nm})}{R(840\text{ nm}) + R(668\text{ nm})} \quad (2)$$

where $R(840\text{nm})$ is the reflectance at 840 nm and $R(668\text{nm})$ is the reflectance at 668 nm.

Table 2. Classes of the model and the number of pixels used to train and validate each class.

Name	Taxonomic Class	Training Pixels	Validation Pixels
Benthic diatoms	Bacillariophyceae	4475	9807
Green macroalgae	Chlorophyceae	17,140	25,910
Seagrass	Magnoliopsida	221,065	179,119
Brown macroalgae	Phaeophyceae	169,936	82,161
Red macroalgae	Rhodophyceae	5771	10,054
Water	-	83,677	76,612
Sediment	-	95,126	57,299

2.4.2. Model Building

A neural network classification model was built using the fastai workflow [50]. This model was composed of two hidden layers and had a total of 26,054 trainable parameters. The parameters have been fine-tuned using 12 epochs to minimize the error rate. This model has been called DISCOV, standing for Drone Intertidal Substrate Classification Of Vegetation.

2.4.3. Validation

The workflow of this study revolves around two distinct flight heights (12 and 120 m, Figure 3), where ensuring consistency between reflectances at both heights is crucial. This comparison was conducted at sites where low and high-altitude flights overlapped. To compare the reflectances of both flights, the low-altitude flights were resampled to the same spatial resolution and grid as the high-altitude flights using a median resampling method. Reflectance values were then extracted, and a scatterplot was generated. The Root Mean Square Error (RMSE) was computed to compare the difference between the raw and standardized reflectance.

The classification model was applied to all flights at both 12 and 120 m of altitude. In situ, information on georeferenced class type and percent cover, acquired over homogeneous vegetation patches at the same time as drone flights, was used to assess the model accuracy. These images were used to construct a validation dataset indicating the presence or absence of each class. In addition, for the quadrat-based validation dataset, polygons of each class were photo-interpreted to increase the number of pixels of the validation dataset. A total of 536,000 pixels were used to validate the Neural Network classifier. The sites with the lowest and highest number of validation data were Gafanha Low (17,316 pixels) and Marinha Lanzarote (159,713 pixels), respectively. A confusion matrix, along with precision metrics such as global accuracy, sensitivity, specificity, F1 score, and Kappa coefficient, were generated for each site.

$$\text{Global accuracy} = \frac{\sum_{i=1}^{k} \text{TP}_i}{\sum_{i=1}^{k} (\text{TP}_i + \text{FP}_i + \text{FN}_i)}$$

$$\text{Sensitivity}_i = \frac{\text{TP}_i}{\text{TP}_i + \text{FN}_i}$$

$$\text{Specificity}_i = \frac{\text{TN}_i}{\text{TN}_i + \text{FP}_i}$$

$$\text{F1}_i = \frac{2 \cdot \text{TP}_i}{2 \cdot \text{TP}_i + \text{FP}_i + \text{FN}_i}$$

All validation matrices were then aggregated to create an overall matrix.

2.5. Variable Importance

Variable Importance Plots (VIP) serve as a method to identify which predictors are important for predicting a specific class. Out of the 21 predictors used in this study, Variable Importance was computed only for the raw and standardized values of the 10 spectral bands captured by the MicaSense camera. This was achieved by repeatedly predicting the same dataset while randomly shuffling one predictor at a time. The benchmark score obtained after each iteration is then compared to the benchmark score obtained without shuffling any variables. The greater the difference between these two benchmark values, the more important the variable is for the model [51].

2.6. Influence of the Spatial Resolution on Classification

To assess the impact of spatial resolution on the model's output, we resampled the drone ortho-mosaics from their native resolution (8 cm for high-altitude flights) using the "average" method from the terra package in R. The rasters were resampled to 32 different resolutions, ranging from 10 cm to 30 m. DISCOV was then applied to these resampled rasters, and the results were compared to the original model predictions. For each resolution and vegetation class, we calculated the predicted area loss, where a score of 0 indicates no area loss during spatial resampling, and a score of 100 indicates complete loss of the vegetation class.

We used a Generalized Linear Model (GLM) with a Beta distribution to examine the relationship between pixel resolution, vegetation class, and their interaction with the loss of vegetation. The loss of vegetation was modeled as a function of the interaction between pixel resolution and vegetation class (Benthic diatoms, brown macroalgae, seagrass, green macroalgae and red macroalgae). Sample vs. fitted residuals and quartile–quartile graphics were assessed visually to ensure that the assumptions of the models used were met.

2.7. Impact of Mixed Vegetation Cover on the Prediction

The key aspect of the workflow adopted in the present study is the mapping at two different altitudes (12 and 120 m), resulting in two distinct resolutions for the same area (8 and 80 mm, respectively). The high-resolution flight was used to estimate the sub-pixel composition for each pixel of the lower-resolution flight. Consequently, within each pixel of the high-altitude flights, the contribution of each vegetation class (% cover) was obtained, and a kernel density plot was generated. This plot provided a visual representation of the model's behavior in mixed vegetation scenarios. It helped to understand the minimum vegetation cover of a given class within a pixel necessary for the model to confidently predict that class.

3. Results

3.1. Reflectance Comparison Between the Two Different Altitudes

In this study, drone flights were conducted at two different altitudes (12 and 120 m) to construct the neural network model. At the sites where the flights at both altitudes overlapped, the reflectance was compared. Overall, there was a good agreement between the two altitudes (RMSE: 0.027; Figure 4).

There was a slight underestimation of raw reflectance values in the high-altitude flight, particularly for higher reflectance values (Figure 4A). Since both flights were conducted over vegetated areas, the highest reflectance values correspond to the infrared part of the spectrum. This difference was not present when the reflectance was standardized (Equation (1); Figure 4B).

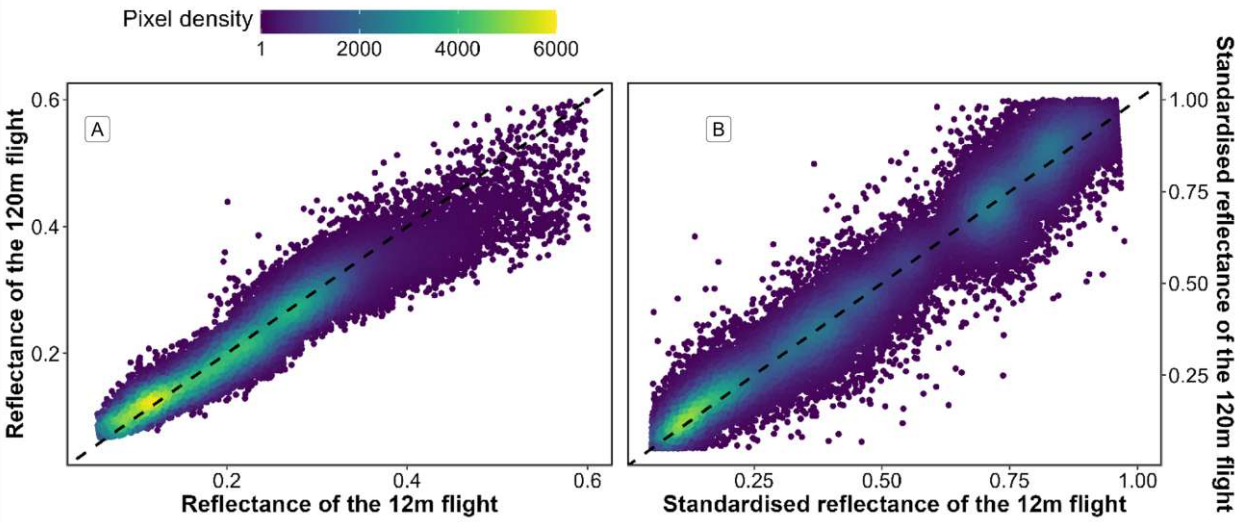

Figure 4. Comparison of reflectance retrieved from both low-altitude and high-altitude flights over a common area. The black dashed line represents a 1 to 1 relationship. The left (**A**) plots raw data, and the right (**B**) plots standardized data (Equation (1)).

3.2. Classification

Each drone flight was used to produce a prediction map, as well as a probability map that indicates the model-derived probability of the selected class for every pixel. The low-altitude flight conducted in Gafanha, Portugal, represented the site with the highest complexity (Figure 5). Four of the five vegetation classes on which the model was trained were present on this site, with green and red macroalgae mixed with a seagrass meadow. There were also benthic diatoms biofilms on the sediment surface. Although the seagrass was solely composed of a single species, *Zostera noltei*, two colors of this species could be observed: dark green (corresponding to healthy leaves) and brown (when leaves are senescent or have an altered pigment composition). Regardless of the variation of color, the class Magnoliopsida (seagrass) was accurately predicted by the model (F1 score of 0.96 at that site).

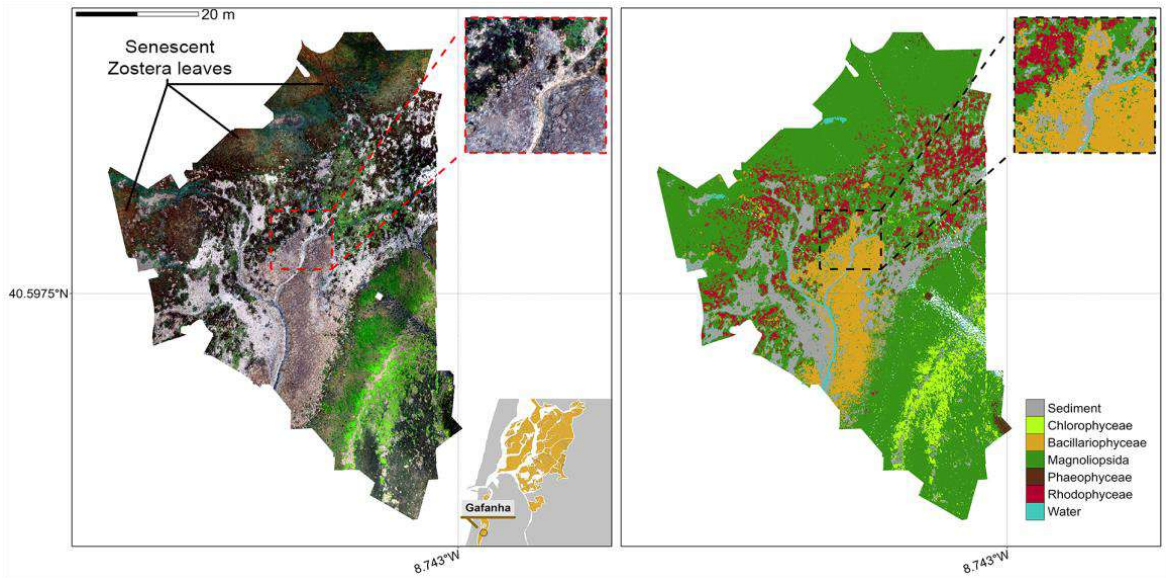

Figure 5. RGB ortho-mosaic (**Left**) and Prediction (**Right**) of the low altitude flight of Gafanha, Portugal. The total extent of this flight was 3000 m^2 with a resolution of 8 mm per pixel. The zoom covers an area equivalent to a 10 m Sentinel-2 pixel size.

The high-altitude flight over Gafanha covered a total area of ~1 km^2 (Figure 6). A channel contouring a small island was masked in the prediction map. Most of the vegetation area was classified as seagrass by the model, including patches with brown leaves. Only a few pixels were classified as green macroalgae (F1 score of 0.55). Patches of red macroalgae were correctly classified (F1 score of 0.85). In the northern part of the site and near the land edges, patches of the halophyte *Sporobolus maritimus* (syn. *Spartina maritima)* were misclassified, either as seagrass or as brown algae (F1 score of 0.77 and 0.71, respectively).

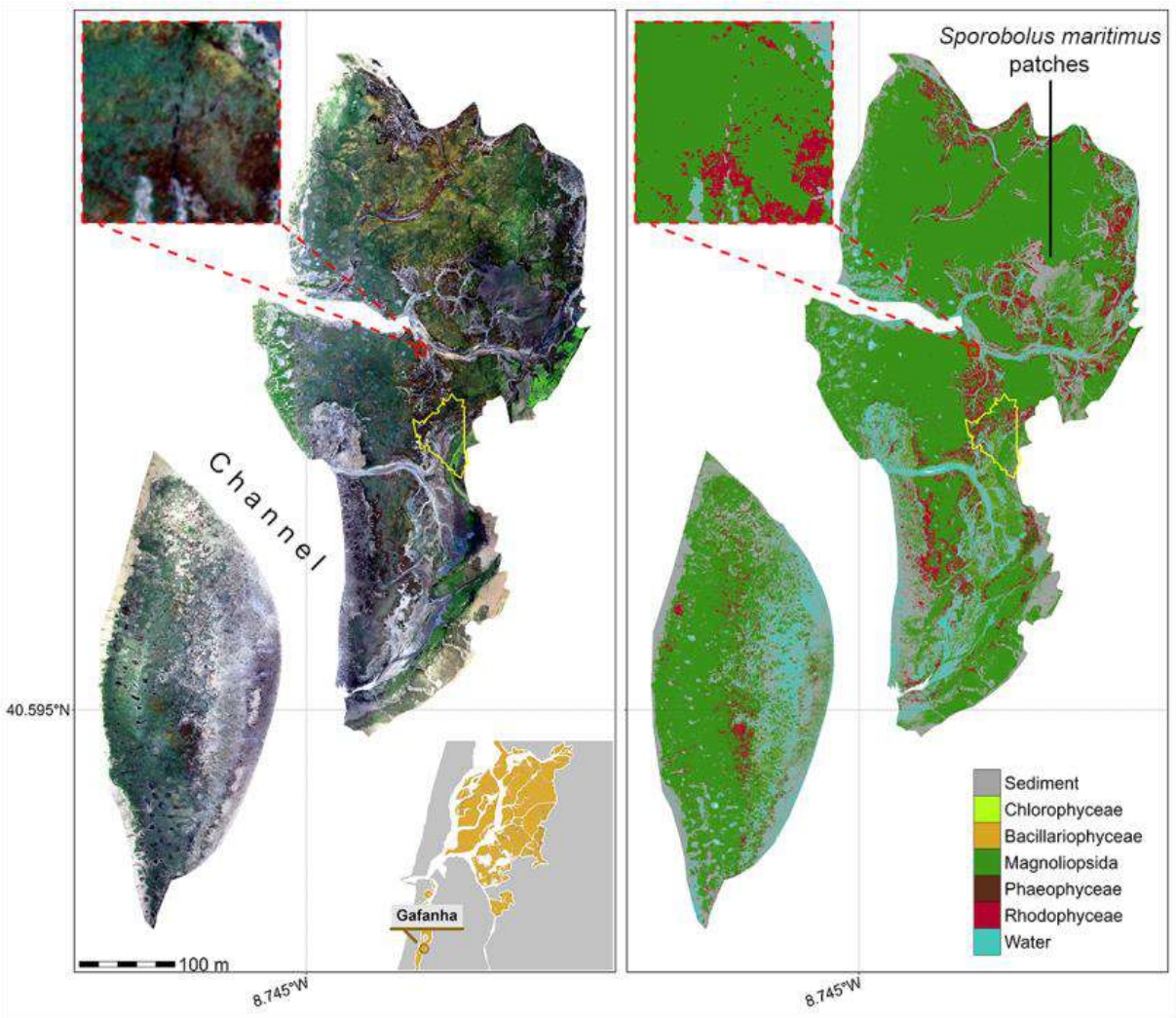

Figure 6. RGB ortho-mosaic (**Left**) and Prediction (**Right**) of the high-altitude flight of Gafanha, Portugal. The total extent of this flight was about 1 km^2 with a resolution of 80 mm per pixel. The yellow outline shows the extent of Gafanha's low-altitude flight, as presented in Figure 5. The zoom covers an area equivalent to a 10 m Sentinel-2 pixel size.

The flight over L'Epine in Noirmoutier Island, France (Figure 8), was conducted near a dike that crossed the northern part of the site from West to East. Alongside this dike, Fucale brown macroalgae (*Fucus* spp., *Ascophyllum nodosum*) were attached to sparse rocks, and stranded green algae (*Ulva* spp.) could be observed, which was correctly reproduced by the prediction (Figure 8 bottom). This site was characterized by a high mixture of green macroalgae and seagrass, but these two classes were correctly discriminated by the classifier (F1 score of 0.97 and 0.98, respectively).

Among the high-altitude flights, the flight acquired over the inner part of Ria de Aveiro coastal lagoon covered the largest area with approximately 1.5 km^2 (Figure 7). The vegetation present at the site was dominated by seagrass and red macroalgae. The

classification provided consistent results, with a patchy seagrass meadow mixed with red macroalgae on the eastern part of the site. As shown in the zoom (Figure 7), the edges of the meadow were mixed with green macroalgae (*Ulva* spp.), which the model agreed with (F1 score of 0.89 for green algae, 0.97 for seagrass and 0.98 for red algae).

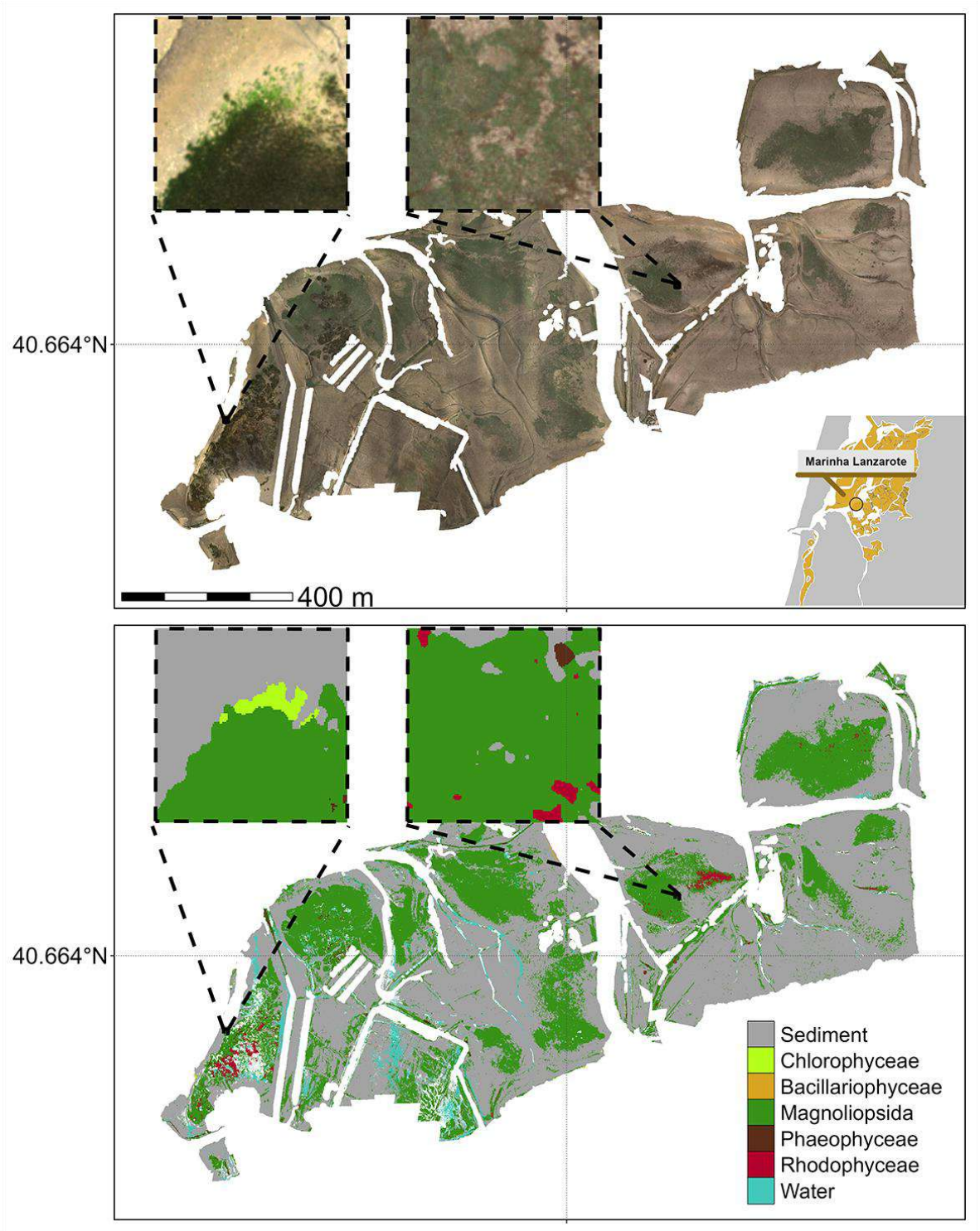

Figure 7. RGB ortho-mosaic (**Top**) and Prediction (**Bottom**) of the flight made in the inner part of Ria de Aveiro coastal lagoon, Portugal. The total extent of this flight was about 1.5 km^2 with a resolution of 80 mm per pixel. The zoom inserts cover an area equivalent to the size of a 10 m Sentinel-2 pixel.

3.3. Validation of the Model

With all drone flights combined, the model's global accuracy was 94.26%, with a Kappa coefficient of 0.92 (Figure 9).

The lowest-performing site was Gafanha High (global accuracy of 75.45%), whereas Mataduços was the site with the most accurate prediction (global accuracy of 98.05%). Overall, the classes Phaeophyceae, Magnoliopsida, Sediment, and Rhodophyceae were correctly classified with a balanced accuracy of 1, 0.96, 0.96, and 0.91, respectively. Bacillariophyceae was the least accurate class (accuracy of 0.72), mainly due to confusion with Magnoliopsida and Sediment.

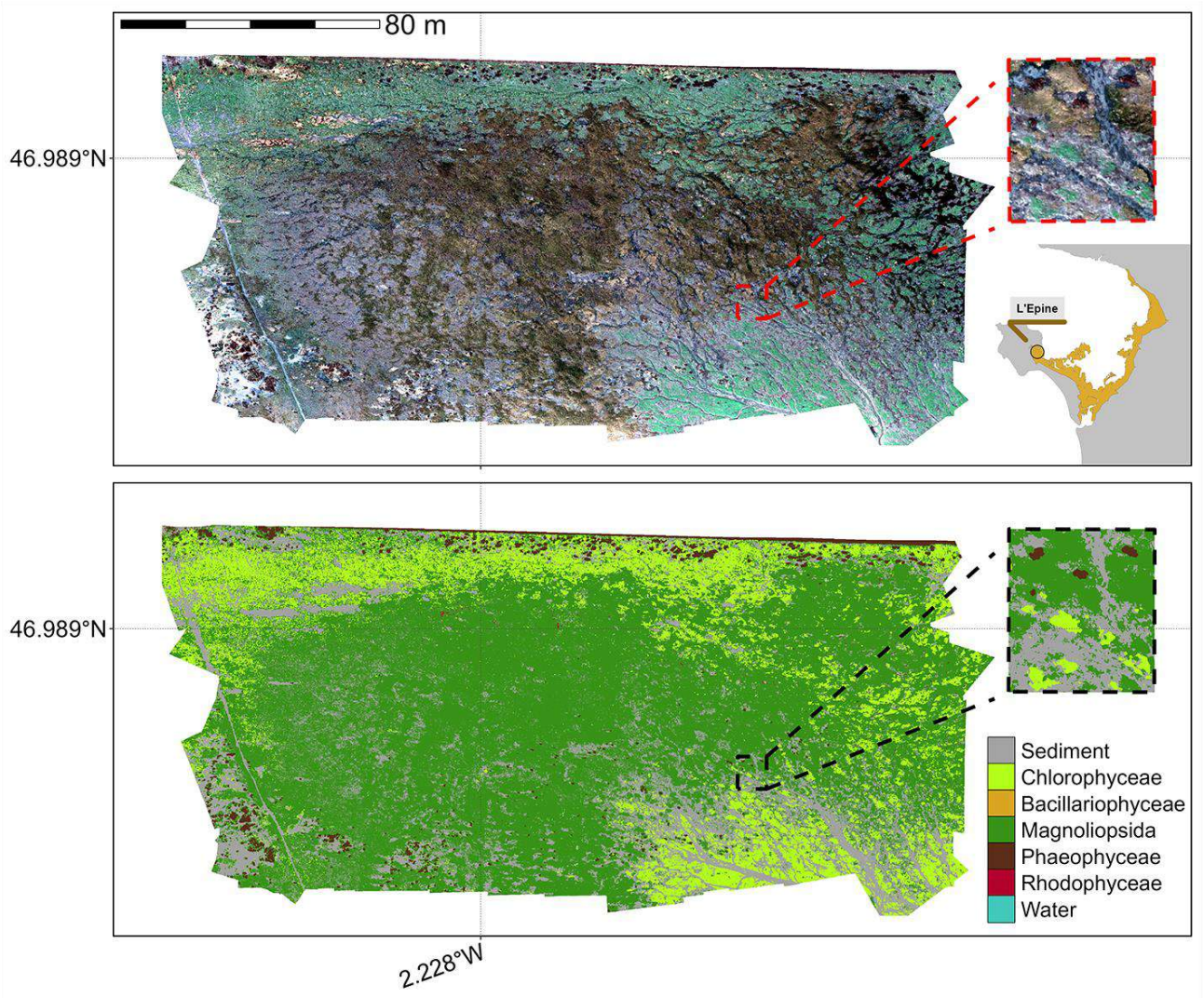

Figure 8. RGB ortho-mosaic (**Top**) and Prediction (**Bottom**) of L'Epine, France. The total extent of this flight was about 28,000 m^2 with a resolution of 80 mm per pixel. The zoom covers an area equivalent to a 10 m Sentinel-2 pixel size.

3.4. Variable Importance Estimation

The computation of variable importance made it possible to identify which bands were the most useful for class prediction (Figure 10).

The spectral bands at 444, 717, and 842 nm of the Micasense camera did not provide important information to discriminate any of the vegetation classes. The band at 531 nm was the most important predictor by far for the classifier to accurately predict Chlorophyceae. In fact, at this wavelength, the Chlorophyceae spectra showed the highest reflectance among all vegetation classes (Figure 10). The bands at 531 and 740 nm were the most

important predictors for Phaeophyceae, corresponding to the lowest reflectance among all classes. Bands at 475 and 560 nm were the most important predictors for Bacillariophyceae and Rhodophyceae, respectively. Four predictors, ranging from the green (560 nm) to the RedEdge (705 nm) bands, were important to accurately predict Magnoliopsida.

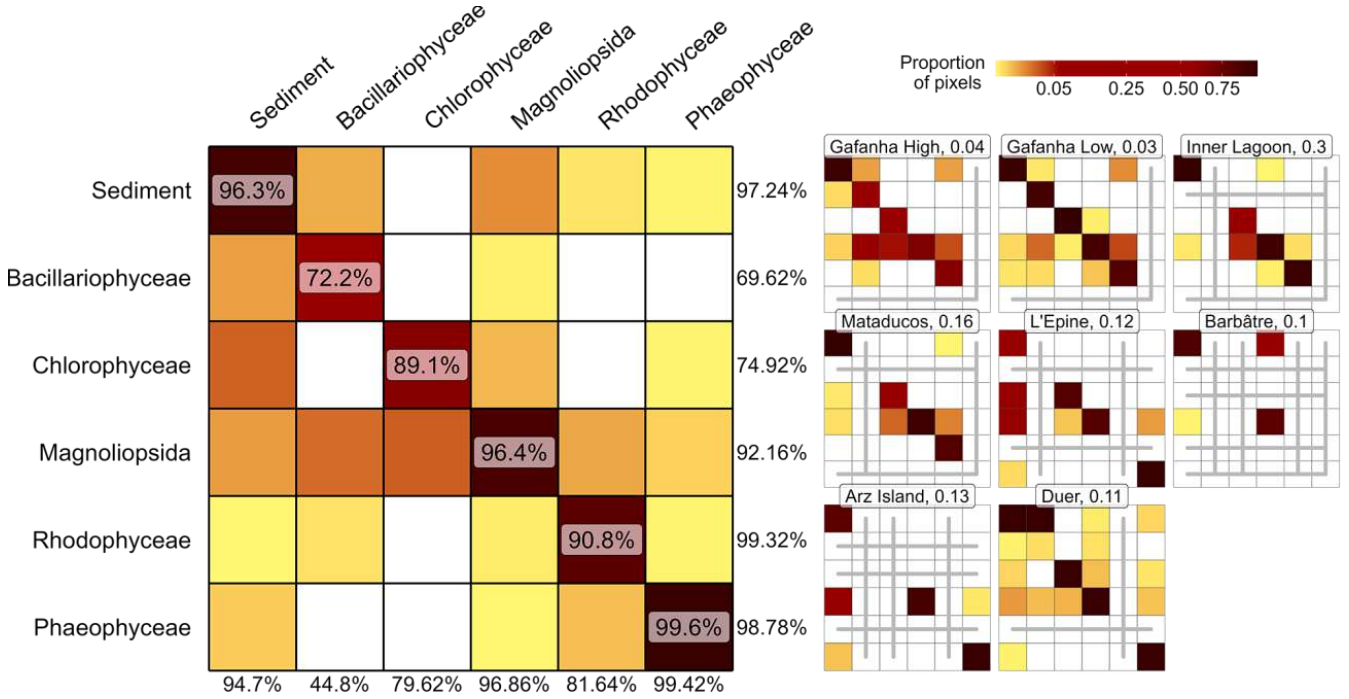

Metrics	Sediment	Bacillariophyceae	Chlorophyceae	Magnoliopsida	Rhodophyceae	Phaeophyceae	Overall
Sensitivity	0.95	0.45	0.8	0.97	0.82	0.99	0.83
Specificity	0.98	1	0.99	0.96	1	1	0.99
Accuracy	0.96	0.72	0.89	0.96	0.91	1	0.94

Figure 9. A global confusion matrix on the left is derived from validation data across each flight, while a mosaic of confusion matrices from individual flights is presented on the right. The labels inside the matrices indicate the balanced accuracy for each class. The labels at the bottom of the global matrix indicate the User's accuracy for each class, and those on the right indicate the Producer's Accuracy. The values adjacent to the names of each site represent the proportion of total pixels from that site contributing to the overall matrix. Grey lines within the mosaic indicate the absence of validation data for the class at that site. The table at the bottom summarizes the Sensitivity, Specificity, and Accuracy for each class and for the overall model.

3.5. Effect of Spatial Resolution on the Classification

Clear differences were seen in vegetation loss across spatial resolutions and vegetation classes (Figure 11). At a fine resolution of 1 m, changes in the retrieved area for each vegetation type are minimal. Green macroalgae show the highest loss, with 1.2% area lost compared to the native resolution (80 mm). As the resolution coarsens to 10 m, vegetation loss becomes more pronounced, with green macroalgae again experiencing the greatest reduction (12% compared to 8 cm) and seagrass showing the smallest loss (1.3%). All green macroalgae have been lost at a resolution of 30 m (100% compared to 8 cm), while seagrass experiences a relatively small reduction of 11%. Brown and red macroalgae show lower declines, with losses at 30 m resolution reaching approximately 37% and 59%, respectively.

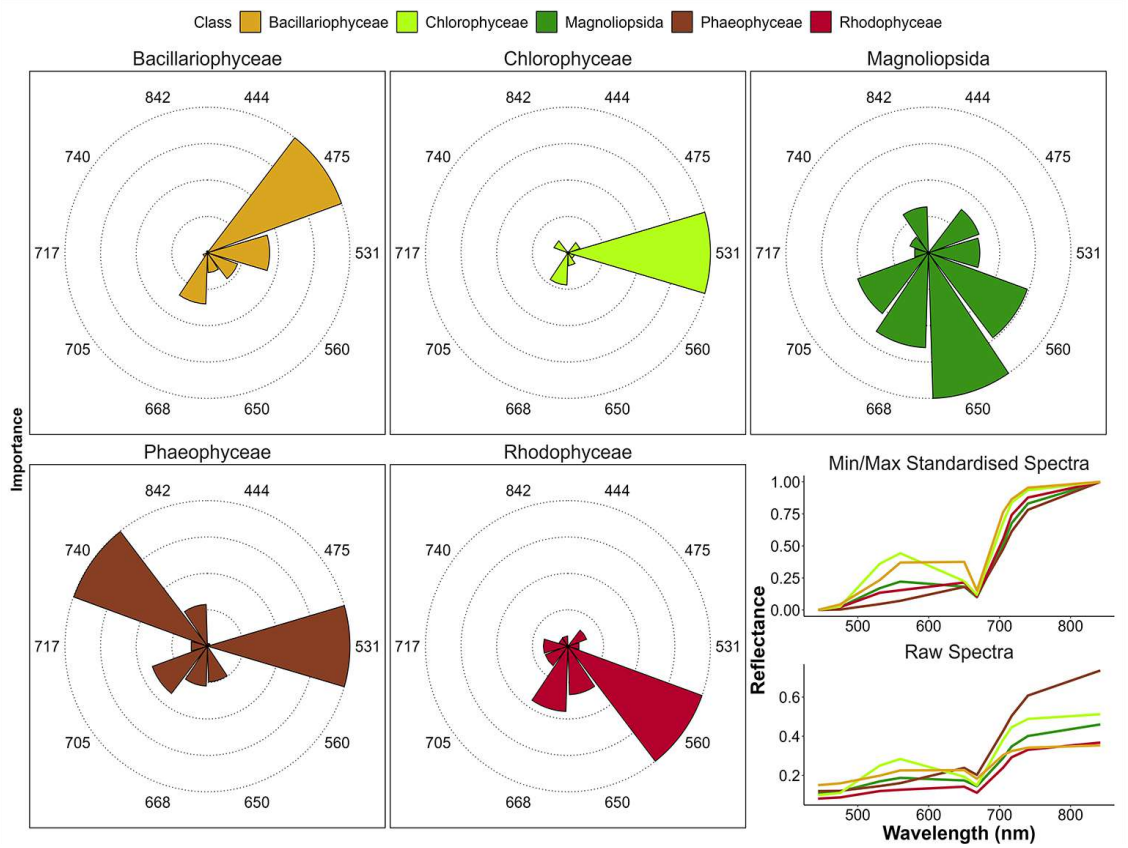

Figure 10. Variable Importance of the Neural Network Classifier for each taxonomic class. The longer the slice, the more important the variable for prediction of each class. The right plot shows the drone raw and standardized reflectance spectra of each class. Each slice represents the Variable Importance (VI) of both raw and standardized reflectance combined.

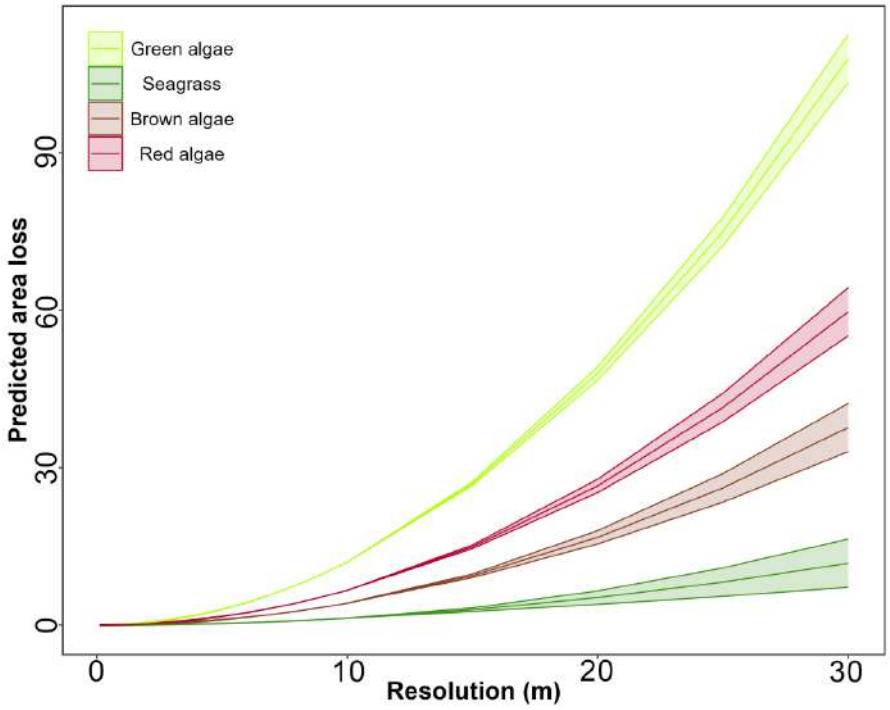

Figure 11. Predicted area loss for different vegetation types (green algae, seagrass, brown algae, and red algae) as a function of spatial resolution. The lines represent Generalized Linear Model (GLM)

predictions, and shaded areas indicate standard errors. As the resolution decreases, predicted area loss increases for all vegetation types, with green algae showing the highest loss and seagrass the smallest at coarser resolutions.

3.6. Effect of the Cover on the Prediction

Using the very high-resolution low-altitude flight (8 mm pixels), we determined the minimal cover (%) required to correctly classify a given class within the corresponding high-altitude flight (8 cm pixel resolution; Figure 12).

A cover of at least 80% was sufficient to have all the 80 mm pixels correctly classified, except for Magnoliopsida, which required a higher cover (>90%) to be accurately classified. Concerning the probability of each class, there is a linear relationship between the percent cover and the confidence of the model to predict the class. To predict green macroalgae with a model likelihood of 0.85, a cover of 93% was needed, 90% for seagrass, 92% for red macroalgae, and 97% for benthic diatoms. When the vegetation cover of a given class was 100%, coarser high-flight pixels were correctly classified for all the classes except for bare sediment, which was only correctly classified 80% of the time. This phenomenon may be attributed to the time gap between the two flights, allowing for microphytobenthos migration to the sediment surface during low tide, consequently altering the model's classification from bare sediment to Bacillariophyceae.

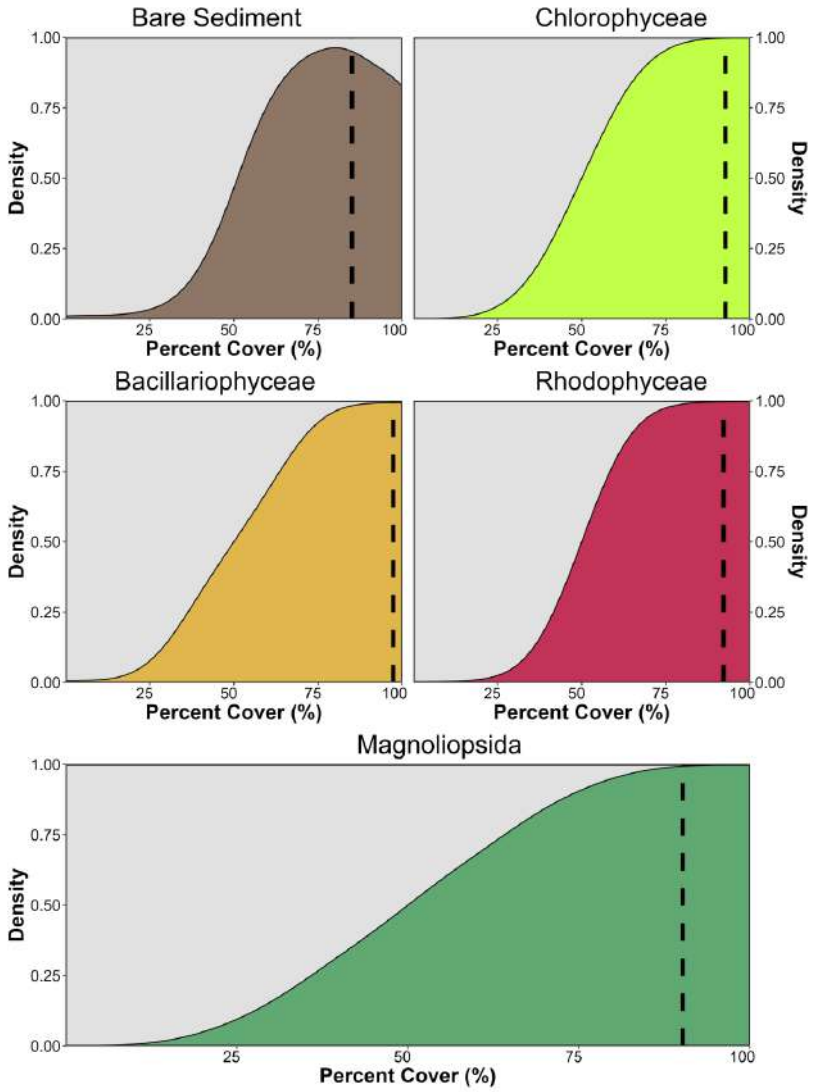

Figure 12. Kernel density plot showing the proportion of pixels well classified based on the percent cover of the class in high-altitude flight pixels of Gafanha, Portugal. Each subplot shows all the pixels

of the same classes on the high-altitude flight. The cover (%) of classes was retrieved using the result of the classification of the low-altitude flight in Gafanha, Portugal.

4. Discussion

4.1. Vegetation Discrimination

The primary objective of this study was to develop a method for the accurate classification of emerged macrophytes observed during low tide on tidal flats, specifically focusing on distinguishing between Chlorophyceae (green macroalgae) and marine Magnoliopsida (seagrasses) using a multispectral resolution. The discrimination between seagrasses and green macroalgae is challenging due to their optical similarity in the visible range [27,52,53]. These two macrophytes share a similar pigment composition: chlorophyll-a (common to all vegetation types), chlorophyll-b (an additional photosynthetic pigment), and accessory carotenoids such as zeaxanthin, lutein and neoxanthin (Figure 13). Their spectral responses could be close, particularly at a multispectral resolution. Seagrass and green macroalgae frequently co-occur in intertidal areas and can intermingle within a remote sensing pixel if the spatial resolution is too low. Here, the issue of intra-pixel mixing was resolved thanks to the very high spatial resolution of the drone (from 8 to 80 mm). In this study, the risk of spectral confusion was avoided by using a machine-learning approach that exploited a neural network classifier. Our drone flights and a recent study based on in situ radiometry suggested that a sensor with at least eight spectral bands ranging from 500 to 850 nm, including a green band at 530 nm and a RedEdge band at 730 nm, was crucial to accurately discriminate green macroalgae from seagrasses [28].

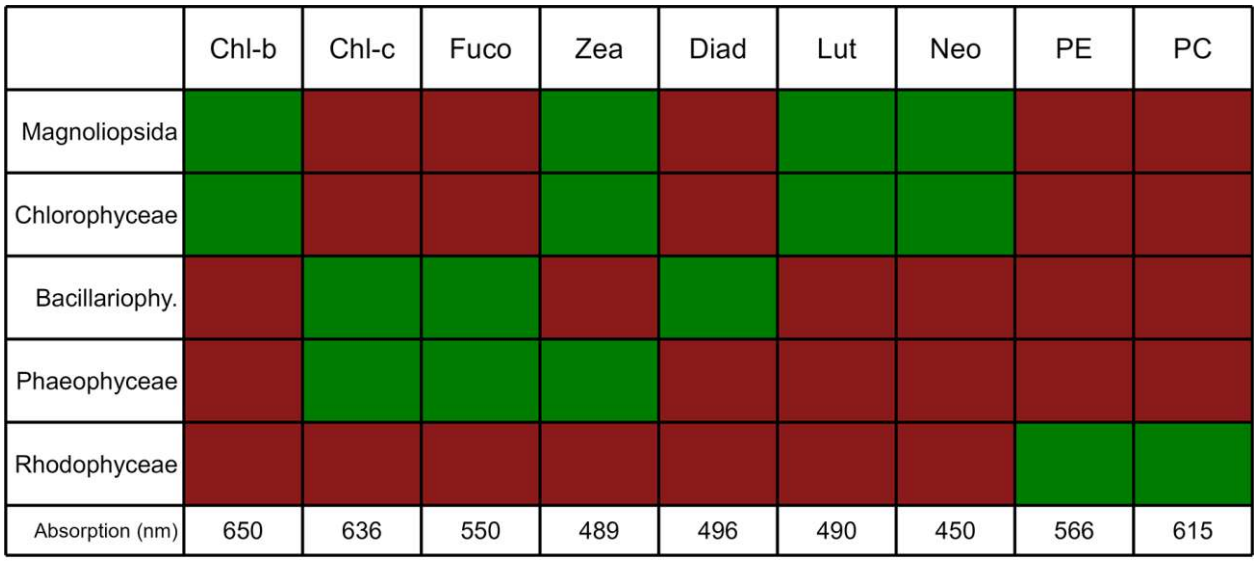

Figure 13. Photosynthetic and carotenoid pigments present (Green) or absent (Red) in each taxonomic class present in the Neural Network Classifier, along with their absorption wavelength measured with spectroradiometer, Chl-b—chlorophyll-b, Chl-c—chlorophyll-c, Fuco—fucoxanthin, Zea—zeaxanthin, Diad—diadinoxanthin, Lut—lutein, Neo—neoxanthin, PE—phycoerythrin, PC—phycocyanin; [25,26,54–56].

Meeting these two criteria, the Micasense RedEdge-MX DUAL camera used in this study enabled the classifier to achieve 97% accuracy between these two classes (Figure 14). Even if their pigment composition is similar, differences in the spectral shape can be observed, with green algae having a higher reflectance peak at 560 nm as well as a higher NIR plateau than seagrass (Figure 2). Such differences were previously attributed to differences in pigments concentration and/or ratios [57], cellular structure as well as in the orientation of the plant at the sediment surface [58–60].

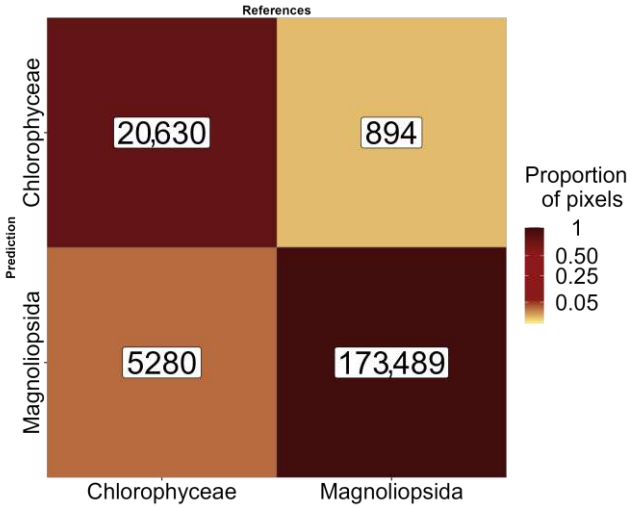

Figure 14. Sample of Figure 9 focusing on green macrophytes. The labels inside the matrix indicate the number of pixels.

The variable importance analysis (Figure 10) identified that the band at 531 nm was the most important for accurately identifying Chlorophyceae. In fact, at this wavelength, Chlorophyceae exhibited the highest reflectance among all other classes, highlighting the difference in carotenoid to chlorophyll-a ratios between seagrasses and green macroalgae [61]. Concerning Phaeophyceae, the thick cell walls of these macroalgae [62] make it more reflective in the infrared part of the spectra [63], while the presence of fucoxanthin and zeaxanthin result in a low reflectance in the visible region (Figures 10 and 13). These two key features have been identified by the Neural Network as the two principal predictors to accurately identify brown algae (Figure 10). Similarly, the presence of phycoerythrin and phycocyanin in Rhodophyceae contributes to the lowest reflectance among all classes in the spectral range from 560 to 615 nm (Figure 10). Indeed, the band at 560 nm has been identified as important for identifying this class, likely due to phycoerythrin absorption at this wavelength. Regarding Bacillariophyceae, 475 nm was the most important predictor for this class (Figure 10). Indeed, the reflectance at 475 nm was higher for Bacillariophyceae than for any other vegetation class (Figure 2), very likely due to the low biomass (and associated concentration of blue-absorbing pigments) of these unicellular organisms compared to seagrass and macroalgae.

4.2. Altitude and Temporal Effects on Vegetation Prediction Accuracy

The ability to differentiate between various types of vegetation plays a critical role in ecological monitoring and coastal management [64]. By distinguishing between seagrasses and macroalgae, our approach facilitates targeted conservation strategies, enabling more effective preservation and restoration efforts in coastal ecosystems. While comparing the reflectance at two different altitudes (12 m and 120 m with a spatial resolution of 8 and 80 mm, respectively), a nearly one-to-one relationship was observed, with a Root Mean Square Error (RMSE) of 0.02 (Figure 4). This result indicates that the reflectance measured by remote sensing (RS) sensors was not significantly influenced by pixel size for these two altitudes. This finding is valuable for integrating drone-based data into larger-scale mapping projects (e.g., combining satellite and drone mapping in side-by-side analyses). The consistency of reflectance across altitudes suggests that drones can be effectively used for finer-scale mapping without compromising data accuracy when merging with other platforms. However, it was observed that there is an underestimation of the infrared part of the spectrum in the high-altitude dataset (Figure 4). Such disparity in infrared reflectance may stem from temporal differences between the flights, possibly resulting in a slightly drier intertidal area and, consequently, higher infrared reflectance. This disparity poses an issue for the methodology followed in the present study, relying solely on one flight

height for training. To address this issue, we employed min/max standardized reflectance spectra as predictors for the model Equation (1). This approach allowed us to eliminate the slight reflectance difference between the flights (Figure 4B) and to focus on the shape of the spectrum in the visible domain (400 to 700 nm). At these wavelengths, different pigments are associated with taxonomic diagnostic features. In contrast to subtidal seagrasses, which maintain relatively constant biomass throughout the year, intertidal seagrasses, like those studied in this work, exhibit strong seasonal phenology [22]. At some sites, they completely disappear during the winter and reach their peak above-ground biomass in the summer and early autumn. Along with these seasonal changes in biomass, the pigment composition and ratios also vary throughout the year, reflecting the plants' adaptations to different environmental conditions [57,65]. Standardization of spectral signatures helps to mitigate the impact of changing biomass on the spectral profile, enabling the development of a model that can reliably predict vegetation across different geographical locations and seasons. This approach allows for consistent classification of vegetation despite variations in biomass and fluctuations in light conditions, providing a robust tool for monitoring and predicting vegetation dynamics [66–68]. However, due to the strong phenology of intertidal seagrass meadows in Europe, the period when a meadow is well-established can be temporally restricted, limiting the ideal window for accurate detection.

4.3. Impact of Pixel Resolution on the Prediction and Implications for Satellite Remote Sensing

Pixel resolution plays a critical role in accurately retrieving vegetation areas from remote sensing data. As pixel size increases, we found a consistent decline in area retrieval across all vegetation types, with more pronounced effects for certain types, such as green macroalgae (Figure 11). This highlights the sensitivity of spatial resolution in detecting smaller or more fragmented vegetation features. Green macroalgae, being particularly patchy across all study sites, showed the steepest decline in areal agreement as pixel size increases, which aligns with expectations given the limitations of coarser resolution in capturing fine-scale details.

This resolution-area relationship has important implications for satellite missions like Sentinel-2 and Landsat, which are commonly used in marine and coastal vegetation studies. Both satellites offer high-resolution imagery, with pixel sizes of 10 m and 30 m, respectively. While these resolutions are suitable for broad-scale environmental monitoring, they may be too coarse to capture finer-scale heterogeneity, as was observed with green macroalgae in this study. Our findings suggest that while the 30 m resolution of Landsat may be adequate for homogeneous vegetation types such as seagrass, a higher resolution is essential for accurately mapping patchy vegetation like green macroalgae. These findings have direct implications for environmental management and conservation planning. Overlooking fine-scale vegetation features such as those seen in green macroalgae could result in inadequate protection or restoration efforts, particularly in ecologically sensitive coastal zones, as the early stages of green tides could be challenging to detect at coarse resolutions.

Very high-resolution imagery offers more accurate vegetation mapping but comes with trade-offs. As resolution increases, data costs rise, and processing becomes more resource-intensive due to the larger file sizes and computational demands. Consequently, high-resolution data requires more storage and can slow down real-time applications. For large-scale monitoring of homogeneous vegetation types, a 10 m resolution of S2/MSI or even 30 m of Landsat/OLI is often sufficient. However, when mapping vegetation like macroalgae with a heterogeneous distribution, the precision provided by higher-resolution imagery is crucial despite the additional costs and processing challenges it imposes.

4.4. Towards Climate and Biodiversity Applications

Climate change, global warming, eutrophication, alien and invasive species development, coastal erosion, and sea level rise are expected to continue impacting coastal ecosystems in the future [69–71] and the demand for meaningful and efficient monitoring of coastal habitats has never been higher [52,72,73]. Our findings, particularly the

improved discrimination of intertidal seagrass and green macroalgae from other intertidal vegetation classes, highlight the potential of drone-based remote sensing to support diverse applications, from the conservation of biodiversity to climate change adaptation strategies.

Due to increasing coastal eutrophication, macroalgal blooms are becoming increasingly common in many regions around the world [74,75]. These blooms can have negative impacts on human health and local economic activities, including, fishing and aquaculture, tourism, and recreational activities [75,76]. The first green tide events (i.e., the bloom of green macroalgae of the genus Ulva) were reported in Brittany, France, in the 1970s and have since been a concern for local stakeholders and economic activities [77]. Some regions of the world have witnessed an increase in brown macroalgae blooms, predominantly involving algae of the genus Sargassum washing along the Caribbean coastlines [78] and, more recently, *Rugulopteryx okamurae* in southern Europe [39]. Satellite remote sensing has proven to be a valuable tool for mapping the spatial and temporal extent of macroalgal blooms worldwide. However, due to limitations in spatial resolution, it can only effectively map well-developed blooms [79–81].

High spatial resolution drone imagery, coupled with an accurate classification algorithm, could be used to map the early stages of macroalgal blooms in areas known to have regular blooms or in new sites. Indeed, this approach could provide early warning alerts to local managers and complement traditional sampling methods to monitor coastal ecosystems. These methods are generally time and resource-intensive, and the findings are often difficult to scale up when applied alone. Earth Observation can bridge this gap and meet the need for systematic monitoring of coastal ecosystems over large areas [82]. The retrieval of Essential Biodiversity Variables and Essential Ocean Variables through satellite observations has been increasingly common, enabling comprehensive monitoring of entire ecosystems over extended time periods [14,83]. The Water Framework Directive [64] mandates the achievement and maintenance of "good ecological status" for all European waters, which necessitates a comprehensive understanding and monitoring of aquatic ecosystems, including coastal habitats like seagrass beds [14,84,85].

Effective and efficient monitoring tools are essential for identifying the impacts of human activities and natural changes on coastal ecosystems. On-demand, multispectral drone observations at very high spatial resolution provide a novel and powerful tool to rapidly and accurately acquire ground truth data, which can be used to develop machine-learning algorithms for satellite sensors [21]. Spatially resolved data are indeed critical for calibrating and validating satellite remote sensing observations, thereby enhancing our capacity to monitor vast coastal areas. The integration of drone technology facilitates a scalable approach to environmental surveillance while taking into account the patchiness of vegetation, offering significant advancements in the spatial and temporal resolution of data collection. This, in turn, supports the EU WFD's objectives by enabling more informed and timely management decisions for the conservation and restoration of aquatic ecosystems.

5. Conclusions

The utilization of very high spatial resolution (from 8 to 80 mm) drone-based remote sensing coupled with machine learning techniques has proven to be an effective method for the discrimination of intertidal seagrasses from green macroalgae with a multispectral resolution sensor. Standardized reflectance was incorporated into the Neural Network model, allowing for a better discrimination of spectral features related to pigment absorption in the visible region of the spectrum. There was a striking difference between the variables of importance in discriminating Magnoliopsida from Chlorophyceae. The latter was essentially identified with the 451 nm spectral band, while more spectral bands were needed to identify the former, notably 650, 560, 668, and 705 nm. As the spectral bands of the Micasense RedEdge Dual sensor are very similar to those of Sentinel-2/MSI, we suggest that multispectral satellite data have the potential to perform this discrimination between these green macrophytes. The findings underscore the importance of adopting advanced remote sensing tools in ecological studies and environmental monitoring, providing a

foundation for future research and policy implementation aimed at ecosystem conservation and restoration.

Author Contributions: Conceptualization, S.O., B.F.R.D., P.G. and L.B.; Methodology, S.O., B.F.R.D., P.R., M.L.Z., P.G. and L.B.; Validation, S.O., B.F.R.D., P.R., P.G. and L.B.; Formal analysis, S.O.; Investigation, S.O., B.F.R.D. and L.B.; Data curation, S.O., B.F.R.D., A.I.S., P.R., M.L.Z., G.B., P.G. and L.B.; Writing—original draft, S.O.; Writing—review & editing, S.O., B.F.R.D., A.I.S., M.L.Z., P.G. and L.B.; Supervision, P.G. and L.B.; Project administration, P.G. and L.B.; Funding acquisition, P.G. and L.B. All authors have read and agreed to the published version of the manuscript.

Funding: This research was funded by BiCOME (Biodiversity of the Coastal Ocean: Monitoring with Earth Observation) project funded by the European Space Agency under the 'Earth Observation Science for Society' element of FutureEO-1 BIODIVERSITY+PRECURSORS call, contract No. 4000135756/21/I-EF; French Ministry of Research & Higher Education; FCT/MCTES (Fundação para a Ciência e a Tecnologia) under the project UIDB/50017/2020 + UIDP/50017/2020 + LA/P/0094/2020 granted to CESAM and through research contract CEECIND/00962/2017 (DOI: 10.54499/CEECIND/00962/2017/CP1459/CT0008); BIOPRADARIA (MAR-01.04.02-FEAMP-0020), funded by the Operational Program MAR2020, EMFF-European Maritime and Fisheries Fund, European Union, Portugal2020.

Data Availability Statement: All code used to create the DISCOV model and apply it to Micasense Dual MX images, as described, are available at https://oirysimon.com/discov (accessed on 19 November 2024).

Acknowledgments: The authors would like to thank the extensive revisions and comments made by anonymous reviewers to improve the work.

Conflicts of Interest: The authors declare no conflict of interest.

References

1. Unsworth, R.K.; Cullen-Unsworth, L.C.; Jones, B.L.; Lilley, R.J. The planetary role of seagrass conservation. *Science* **2022**, *377*, 609–613. [CrossRef] [PubMed]
2. Sousa, A.I.; da Silva, J.F.; Azevedo, A.; Lillebø, A.I. Blue carbon stock in *Zostera noltei* meadows at ria de aveiro coastal lagoon (Portugal) over a decade. *Sci. Rep.* **2019**, *9*, 14387. [CrossRef]
3. Gardner, R.C.; Finlayson, C. *Global Wetland Outlook: State of the World's Wetlands and Their Services to People*; Stetson Law; Secretariat of the Ramsar Convention: Gland, Switzerland, 2018; p. 88.
4. Jankowska, E.; Michel, L.N.; Lepoint, G.; Włodarska-Kowalczuk, M. Stabilizing effects of seagrass meadows on coastal water benthic food webs. *J. Exp. Mar. Biol. Ecol.* **2019**, *510*, 54–63. [CrossRef]
5. Zoffoli, M.L.; Gernez, P.; Oiry, S.; Godet, L.; Dalloyau, S.; Davies, B.F.R.; Barillé, L. Remote sensing in seagrass ecology: Coupled dynamics between migratory herbivorous birds and intertidal meadows observed by satellite during four decades. *Remote Sens. Ecol. Conserv.* **2022**, *9*, 420–433. [CrossRef]
6. Chefaoui, R.M.; Duarte, C.M.; Serrão, E.A. Dramatic loss of seagrass habitat under projected climate change in the mediterranean sea. *Glob. Change Biol.* **2018**, *24*, 4919–4928. [CrossRef] [PubMed]
7. Duffy, J.E.; Benedetti-Cecchi, L.; Trinanes, J.; Muller-Karger, F.E.; Ambo-Rappe, R.; Boström, C.; Buschmann, A.H.; Byrnes, J.; Coles, R.G.; Creed, J.; et al. Toward a coordinated global observing system for seagrasses and marine macroalgae. *Front. Mar. Sci.* **2019**, *6*, 317. [CrossRef]
8. Lin, H.; Sun, T.; Zhou, Y.; Gu, R.; Zhang, X.; Yang, W. Which genes in a typical intertidal seagrass (*Zostera japonica*) indicate copper-, lead-, and cadmium pollution? *Front. Plant Sci.* **2018**, *9*, 1545. [CrossRef]
9. Nguyen, H.M.; Ralph, P.J.; Marín-Guirao, L.; Pernice, M.; Procaccini, G. Seagrasses in an era of ocean warming: A review. *Biol. Rev.* **2021**, *96*, 2009–2030. [CrossRef]
10. Orth, R.J.; Carruthers, T.J.; Dennison, W.C.; Duarte, C.M.; Fourqurean, J.W.; Heck, K.L.; Hughes, A.R.; Kendrick, G.A.; Kenworthy, W.J.; Olyarnik, S.; et al. A global crisis for seagrass ecosystems. *Bioscience* **2006**, *56*, 987–996. [CrossRef]
11. Rasheed, M.A.; Unsworth, R.K. Long-term climate-associated dynamics of a tropical seagrass meadow: Implications for the future. *Mar. Ecol. Prog. Ser.* **2011**, *422*, 93–103. [CrossRef]
12. Soissons, L.M.; Haanstra, E.P.; Van Katwijk, M.M.; Asmus, R.; Auby, I.; Barillé, L.; Brun, F.G.; Cardoso, P.G.; Desroy, N.; Fournier, J.; et al. Latitudinal patterns in european seagrass carbon reserves: Influence of seasonal fluctuations versus short-term stress and disturbance events. *Front. Plant Sci.* **2018**, *9*, 88. [CrossRef] [PubMed]
13. de Los Santos, C.B.; Krause-Jensen, D.; Alcoverro, T.; Marbà, N.; Duarte, C.M.; Van Katwijk, M.M.; Pérez, M.; Romero, J.; Sánchez-Lizaso, J.L.; Roca, G.; et al. Recent trend reversal for declining european seagrass meadows. *Nat. Commun.* **2019**, *10*, 3356. [CrossRef] [PubMed]

14. Zoffoli, M.L.; Gernez, P.; Godet, L.; Peters, S.; Oiry, S.; Barillé, L. Decadal increase in the ecological status of a north-atlantic intertidal seagrass meadow observed with multi-mission satellite time-series. *Ecol. Indic.* **2021**, *130*, 108033. [CrossRef]
15. Devlin, M.; Brodie, J. Nutrients and eutrophication. In *Marine Pollution–Monitoring, Management and Mitigation*; Springer: Berlin/Heidelberg, Germany, 2023; pp. 75–100.
16. Wang, Z.; Fang, Z.; Liang, J.; Song, X. Assessment of global habitat suitability and risk of ocean green tides. *Harmful Algae* **2022**, *119*, 102324. [CrossRef]
17. Miloslavich, P.; Bax, N.J.; Simmons, S.E.; Klein, E.; Appeltans, W.; Aburto-Oropeza, O.; Garcia, M.A.; Batten, S.D.; Benedetti-Cecchi, L.; Checkley, D.M.; et al. Essential ocean variables for global sustained observations of biodiversity and ecosystem changes. *Glob. Change Biol.* **2018**, *24*, 2416–2433. [CrossRef]
18. Pereira, H.M.; Ferrier, S.; Walters, M.; Geller, G.N.; Jongman, R.H.; Scholes, R.J.; Bruford, M.W.; Brummitt, N.; Butchart, S.H.; Cardoso, A.; et al. Ecology. Essential biodiversity variables. *Science* **2013**, *339*, 277–278.
19. Nijland, W.; Reshitnyk, L.; Rubidge, E. Satellite remote sensing of canopy-forming kelp on a complex coastline: A novel procedure using the landsat image archive. *Remote Sens. Environ.* **2019**, *220*, 41–50. [CrossRef]
20. Coffer, M.M.; Graybill, D.D.; Whitman, P.J.; Schaeffer, B.A.; Salls, W.B.; Zimmerman, R.C.; Hill, V.; Lebrasse, M.C.; Li, J.; Keith, D.J.; et al. Providing a framework for seagrass mapping in united states coastal ecosystems using high spatial resolution satellite imagery. *J. Environ. Manag.* **2023**, *337*, 117669. [CrossRef]
21. Davies, B.F.R.; Oiry, S.; Rosa, P.; Zoffoli, M.L.; Sousa, A.I.; Thomas, O.R.; Smale, D.A.; Austen, M.C.; Biermann, L.; Attrill, M.J.; et al. A sentinel watching over inter-tidal seagrass phenology across western europe and north africa. *Commun. Earth Environ.* **2024**, *5*, 382. [CrossRef]
22. Davies, B.F.R.; Oiry, S.; Rosa, P.; Zoffoli, M.L.; Sousa, A.I.; Thomas, O.R.; Smale, D.A.; Austen, M.C.; Biermann, L.; Attrill, M.J.; et al. Intertidal seagrass extent from sentinel-2 time-series show distinct trajectories in western europe. *Remote Sens. Environ.* **2024**, *312*, 114340. [CrossRef]
23. Traganos, D.; Reinartz, P. Mapping mediterranean seagrasses with sentinel-2 imagery. *Mar. Pollut. Bull.* **2018**, *134*, 197–209. [CrossRef] [PubMed]
24. Xu, S.; Xu, S.; Zhou, Y.; Yue, S.; Zhang, X.; Gu, R.; Zhang, Y.; Qiao, Y.; Liu, M. Long-term changes in the unique and largest seagrass meadows in the bohai sea (China) using satellite (1974–2019) and sonar data: Implication for conservation and restoration. *Remote Sens.* **2021**, *13*, 856. [CrossRef]
25. Douay, F.; Verpoorter, C.; Duong, G.; Spilmont, N.; Gevaert, F. New hyperspectral procedure to discriminate intertidal macroalgae. *Remote Sens.* **2022**, *14*, 346. [CrossRef]
26. Ralph, P.; Polk, S.; Moore, K.; Orth, R.; Smith Jr, W. Operation of the xanthophyll cycle in the seagrass *Zostera marina* in response to variable irradiance. *J. Exp. Mar. Biol. Ecol.* **2002**, *271*, 189–207. [CrossRef]
27. Bannari, A.; Ali, T.S.; Abahussain, A. The capabilities of sentinel-MSI (2A/2B) and landsat-OLI (8/9) in seagrass and algae species differentiation using spectral reflectance. *Ocean Sci.* **2022**, *18*, 361–388. [CrossRef]
28. Davies, B.F.R.; Gernez, P.; Geraud, A.; Oiry Simon Rosa, P.; Zoffoli, M.L.; Barillé, L. Multi- and hyperspectral classification of soft-bottom intertidal vegetation using a spectral library for coastal biodiversity remote sensing. *Remote Sens. Environ.* **2023**, *290*, 113554. [CrossRef]
29. Tuya, F.; Hernandez-Zerpa, H.; Espino, F.; Haroun, R. Drastic decadal decline of the seagrass cymodocea nodosa at gran canaria (eastern atlantic): Interactions with the green algae caulerpa prolifera. *Aquat. Bot.* **2013**, *105*, 1–6. [CrossRef]
30. Fairley, I.; Williamson, B.J.; McIlvenny, J.; King, N.; Masters, I.; Lewis, M.; Neill, S.; Glasby, D.; Coles, D.; Powell, B.; et al. Drone-based large-scale particle image velocimetry applied to tidal stream energy resource assessment. *Renew. Energy* **2022**, *196*, 839–855. [CrossRef]
31. Oh, J.; Kim, D.; Lee, H. Use of a drone for mapping and time series image acquisition of tidal zones. *J. Korean Inst. Intell. Syst.* **2017**, *27*, 119–125.
32. Adade, R.; Aibinu, A.M.; Ekumah, B.; Asaana, J. Unmanned aerial vehicle (UAV) applications in coastal zone management—A review. *Environ. Monit. Assess.* **2021**, *193*, 154. [CrossRef]
33. Angnuureng, D.B.; Brempong, K.; Jayson-Quashigah, P.; Dada, O.; Akuoko, S.; Frimpomaa, J.; Mattah, P.; Almar, R. Satellite, drone and video camera multi-platform monitoring of coastal erosion at an engineered pocket beach: A showcase for coastal management at elmina bay, ghana (west africa). *Reg. Stud. Mar. Sci.* **2022**, *53*, 102437. [CrossRef]
34. Casella, E.; Drechsel, J.; Winter, C.; Benninghoff, M.; Rovere, A. Accuracy of sand beach topography surveying by drones and photogrammetry. *Geo-Mar. Lett.* **2020**, *40*, 255–268. [CrossRef]
35. Lange, T.; Oncken, N.S.; Svane, N.; Steinfurth, R.C.; Kristensen, E.; Flindt, M.R. Large-scale eelgrass transplantation: A measure for carbon and nutrient sequestration in estuaries. *Mar. Ecol. Prog. Ser.* **2022**, *685*, 97–109. [CrossRef]
36. Svane, N.; Lange, T.; Egemose, S.; Dalby, O.; Thomasberger, A.; Flindt, M.R. Unoccupied aerial vehicle-assisted monitoring of benthic vegetation in the coastal zone enhances the quality of ecological data. *Prog. Phys. Geogr. Earth Environ.* **2022**, *46*, 232–249. [CrossRef]
37. Brunier, G.; Oiry, S.; Gruet, Y.; Dubois, S.F.; Barillé, L. Topographic analysis of intertidal polychaete reefs (*Sabellaria alveolata*) at a very high spatial resolution. *Remote Sens.* **2022**, *14*, 307. [CrossRef]
38. Joyce, K.E.; Fickas, K.C.; Kalamandeen, M. The unique value proposition for using drones to map coastal ecosystems. *Camb. Prism.Coast. Futures* **2023**, *1*, e6. [CrossRef]

39. Roca, M.; Dunbar, M.B.; Román, A.; Caballero, I.; Zoffoli, M.L.; Gernez, P.; Navarro, G. Monitoring the marine invasive alien species rugulopteryx okamurae using unmanned aerial vehicles and satellites. *Front. Mar. Sci.* **2022**, *9*, 1004012. [CrossRef]
40. Román, A.; Tovar-Sánchez, A.; Olivé, I.; Navarro, G. Using a UAV-mounted multispectral camera for the monitoring of marine macrophytes. *Front. Mar. Sci.* **2021**, *8*, 722698. [CrossRef]
41. Tallam, K.; Nguyen, N.; Ventura, J.; Fricker, A.; Calhoun, S.; O'Leary, J.; Fitzgibbons, M.; Robbins, I.; Walter, R.K. Application of deep learning for classification of intertidal eelgrass from drone-acquired imagery. *Remote Sens.* **2023**, *15*, 2321. [CrossRef]
42. Collin, A.; Dubois, S.; James, D.; Houet, T. Improving intertidal reef mapping using UAV surface, red edge, and near-infrared data. *Drones* **2019**, *3*, 67. [CrossRef]
43. Rossiter, T.; Furey, T.; McCarthy, T.; Stengel, D.B. UAV-mounted hyperspectral mapping of intertidal macroalgae. *Estuar. Coast. Shelf Sci.* **2020**, *242*, 106789. [CrossRef]
44. Zoffoli, M.L.; Gernez, P.; Rosa, P.; Le Bris, A.; Brando, V.E.; Barillé, A.-L.; Harin, N.; Peters, S.; Poser, K.; Spaias, L.; et al. Sentinel-2 remote sensing of *Zostera* noltei-dominated intertidal seagrass meadows. *Remote Sens. Environ.* **2020**, *251*, 112020. [CrossRef]
45. Sousa, A.I.; Santos, D.B.; Silva EF da Sousa, L.P.; Cleary, D.F.; Soares, A.M.; Lillebø, A.I. 'Blue carbon' and nutrient stocks of salt marshes at a temperate coastal lagoon (ria de aveiro, Portugal). *Sci. Rep.* **2017**, *7*, 41225. [CrossRef] [PubMed]
46. Román, A.; Oiry, S.; Davies, B.F.; Rosa, P.; Gernez, P.; Tovar-Sánchez, A.; Navarro, G.; Méléder, V.; Barillé, L. Mapping intertidal microphytobenthic biomass with very high-resolution remote sensing imagery in an estuarine system. *Sci. Total Environ.* **2024**, *955*, 177025. [CrossRef] [PubMed]
47. Davies, B.F.R.; Sousa, A.I.; Figueira, R.; Oiry, S.; Gernez, P.; Barillé, L. Benthic intertidal vegetation from the tagus estuary and aveiro lagoon. In *Sampling Event Dataset*; Université de Nantes: Nantes, France, 2023. [CrossRef]
48. Nebel, S.; Beege, M.; Schneider, S.; Rey, G.D. A review of photogrammetry and photorealistic 3D models in education from a psychological perspective. *Front. Educ.* **2020**, *5*, 1–15. [CrossRef]
49. Cao, J.; Thorson, J.T.; Richards, R.A.; Chen, Y. Spatiotemporal index standardization improves the stock assessment of northern shrimp in the gulf of maine. *Can. J. Fish. Aquat. Sci.* **2017**, *74*, 1781–1793. [CrossRef]
50. Howard, J.; Gugger, S. Fastai: A layered API for deep learning. *Information* **2020**, *11*, 108. [CrossRef]
51. Wei, P.; Lu, Z.; Song, J. Variable importance analysis: A comprehensive review. *Reliab. Eng. Syst. Saf.* **2015**, *142*, 399–432. [CrossRef]
52. Oiry, S.; Barillé, L. Using sentinel-2 satellite imagery to develop microphytobenthos-based water quality indices in estuaries. *Ecol. Indic.* **2021**, *121*, 107184. [CrossRef]
53. Veettil, B.K.; Ward, R.D.; Lima, M.D.A.C.; Stankovic, M.; Hoai, P.N.; Quang, N.X. Opportunities for seagrass research derived from remote sensing: A review of current methods. *Ecol. Indic.* **2020**, *117*, 106560. [CrossRef]
54. Cartaxana, P.; Cruz, S.; Gameiro, C.; Kühl, M. Regulation of intertidal microphytobenthos photosynthesis over a diel emersion period is strongly affected by diatom migration patterns. *Front. Microbiol.* **2016**, *7*, 872. [CrossRef] [PubMed]
55. Christensen, T.; Dixon, P.S.; Irvine, L.M. *Seaweeds of the British Isles: Tribophyceae (Xanthophyceae)*; British Museum (Nat. Hist.): London, UK, 1977.
56. Méléder, V.; Laviale, M.; Jesus, B.; Mouget, J.L.; Lavaud, J.; Kazemipour, F.; Launeau, P.; Barillé, L. In vivo estimation of pigment composition and optical absorption cross-section by spectroradiometry in four aquatic photosynthetic micro-organisms. *J. Photochem. Photobiol. B Biol.* **2013**, *129*, 115–124. [CrossRef] [PubMed]
57. Bargain, A.; Robin, M.; Méléder, V.; Rosa, P.; Le Menn, E.; Harin, N.; Barillé, L. Seasonal spectral variation of *Zostera noltii* and its influence on pigment-based vegetation indices. *J. Exp. Mar. Biol. Ecol.* **2013**, *446*, 86–94. [CrossRef]
58. Beach, K.; Borgeas, H.; Nishimura, N.; Smith, C. In vivo absorbance spectra and the ecophysiology of reef macroalgae. *Coral Reefs* **1997**, *16*, 21–28. [CrossRef]
59. Hedley, J.D.; Mirhakak, M.; Wentworth, A.; Dierssen, H.M. Influence of three-dimensional coral structures on hyperspectral benthic reflectance and water-leaving reflectance. *Appl. Sci.* **2018**, *8*, 2688. [CrossRef]
60. Kirk, J.T. *Light and Photosynthesis in Aquatic Ecosystems*; Cambridge University Press: Cambridge, UK, 1994.
61. Repolho, T.; Duarte, B.; Dionísio, G.; Paula, J.R.; Lopes, A.R.; Rosa, I.C.; Grilo, T.F.; Caçador, I.; Calado, R.; Rosa, R. Seagrass ecophysiological performance under ocean warming and acidification. *Sci. Rep.* **2017**, *7*, 41443. [CrossRef]
62. Charrier, B.; Boscq, S.; Nelson, B.J.; Läubli, N.F. Growth and labelling of cell wall components of the brown alga *Ectocarpus* in microfluidic chips. *Front. Mar. Sci.* **2021**, *8*, 745654. [CrossRef]
63. Slaton, M.R.; Raymond Hunt, E., Jr.; Smith, W.K. Estimating near-infrared leaf reflectance from leaf structural characteristics. *Am. J. Bot.* **2001**, *88*, 278–284. [CrossRef]
64. European-Commission. EU Water Framework Directive. *EC Dir.* **2000**, *60*.
65. Légaré, B.; Bélanger, S.; Singh, R.K.; Bernatchez, P.; Cusson, M. Remote sensing of coastal vegetation phenology in a cold temperate intertidal system: Implications for classification of coastal habitats. *Remote Sens.* **2022**, *14*, 3000. [CrossRef]
66. Costa, V.; Serôdio, J.; Lillebø, A.I.; Sousa, A.I. Use of hyperspectral reflectance to non-destructively estimate seagrass *Zostera noltei* biomass. *Ecol. Indic.* **2021**, *121*, 107018. [CrossRef]
67. Fyfe, S. Spatial and temporal variation in spectral reflectance: Are seagrass species spectrally distinct? *Limnol. Oceanogr.* **2003**, *48*, 464–479. [CrossRef]

68. Piaser, E.; Berton, A.; Bolpagni, R.; Caccia, M.; Castellani, M.B.; Coppi, A.; Dalla Vecchia, A.; Gallivanone, F.; Sona, G.; Villa, P. Impact of radiometric variability on ultra-high resolution hyperspectral imagery over aquatic vegetation: Preliminary results. *IEEE J. Sel. Top. Appl. Earth Obs. Remote Sens.* **2023**, *16*, 5935–5950. [CrossRef]
69. Holon, F.; Marre, G.; Parravicini, V.; Mouquet, N.; Bockel, T.; Descamp, P.; Tribot, A.-S.; Boissery, P.; Deter, J. A predictive model based on multiple coastal anthropogenic pressures explains the degradation status of a marine ecosystem: Implications for management and conservation. *Biol. Conserv.* **2018**, *222*, 125–135. [CrossRef]
70. Marquet, P.A.; Buschmann, A.H.; Corcoran, D.; Díaz, P.A.; Fuentes-Castillo, T.; Garreaud, R.; Pliscoff, P.; Salazar, A. Global change and acceleration of anthropic pressures on patagonian ecosystems. In *Conservation in Chilean Patagonia: Assessing the State of Knowledge, Opportunities, and Challenges*; Springer International Publishing: Cham, Switzerland, 2024; pp. 33–65.
71. Schibalski, A.; Kleyer, M.; Maier, M.; Schröder, B. Spatiotemporally explicit prediction of future ecosystem service provisioning in response to climate change, sea level rise, and adaptation strategies. *Ecosyst. Serv.* **2022**, *54*, 101414. [CrossRef]
72. Muller-Karger, F.E.; Hestir, E.; Ade, C.; Turpie, K.; Roberts, D.A.; Siegel, D.; Miller, R.J.; Humm, D.; Izenberg, N.; Keller, M.; et al. Satellite sensor requirements for monitoring essential biodiversity variables of coastal ecosystems. *Ecol. Appl.* **2018**, *28*, 749–760. [CrossRef]
73. Villalobos Perna, P.; Di Febbraro, M.; Carranza, M.L.; Marzialetti, F.; Innangi, M. Remote sensing and invasive plants in coastal ecosystems: What we know so far and future prospects. *Land* **2023**, *12*, 341. [CrossRef]
74. Sutton, M.A.; Van Grinsven, H.; Billen, G.; Bleeker, A.; Bouwman, A.; Oenema, O. European nitrogen assessement-summary for policy makers. In *The European Nitrogen Assessment: Sources, Effects and Policy Perspectives*; Cambridge University Press: Cambridge, UK, 2011.
75. Ye, N.; Zhang, X.; Mao, Y.; Liang, C.; Xu, D.; Zou, J.; Zhuang, Z.; Wang, Q. "Green tides" are overwhelming the coastline of our blue planet: Taking the world's largest example. *Ecol. Res.* **2011**, *26*, 477–485. [CrossRef]
76. Villares, R.; Puente, X.; Carballeira, A. Nitrogen and phosphorus in ulva sp. In the galician rias bajas (northwest spain): Seasonal fluctuations and influence on growth. *Bol.-Inst. Español Oceanogr.* **1999**, *15*, 337–342.
77. Ménesguen, A. *Les Marées Vertes: 40 Clés Pour Comprendre*; Editions Quae: Plouzané, France, 2018.
78. Louime, C.; Fortune, J.; Gervais, G. Sargassum invasion of coastal environments: A growing concern. *Am. J. Environ. Sci.* **2017**, *13*, 58–64. [CrossRef]
79. Haro, S.; Jimenez-Reina, J.; Bermejo, R.; Morrison, L. BioIntertidal mapper software: A satellite approach for NDVI-based intertidal habitat mapping. *SoftwareX* **2023**, *24*, 101520. [CrossRef]
80. Klemas, V. Remote sensing of algal blooms: An overview with case studies. *J. Coast. Res.* **2012**, *28*, 34–43. [CrossRef]
81. Schreyers, L.; van Emmerik, T.; Biermann, L.; Le Lay, Y.-F. Spotting green tides over brittany from space: Three decades of monitoring with landsat imagery. *Remote Sens.* **2021**, *13*, 1408. [CrossRef]
82. Papathanasopoulou, E.; Simis, S.; Alikas, K.; Ansper, A.; Anttila, J.; Barillé, A.; Barillé, L.; Brando, V.; Bresciani, M.; Bučas, M.; et al. Satellite-assisted monitoring of water quality to support the implementation of the water framework directive. *EOMORES White Paper Zenodo*. 2019. Available online: https://zenodo.org/records/3463051 (accessed on 19 November 2024).
83. Ratnarajah, L.; Abu-Alhaija, R.; Atkinson, A.; Batten, S.; Bax, N.J.; Bernard, K.S.; Canonico, G.; Cornils, A.; Everett, J.D.; Grigoratou, M.; et al. Monitoring and modelling marine zooplankton in a changing climate. *Nat. Commun.* **2023**, *14*, 564. [CrossRef]
84. Foden, J.; Brazier, D. Angiosperms (seagrass) within the EU water framework directive: A UK perspective. *Mar. Pollut. Bull.* **2007**, *55*, 181–195. [CrossRef]
85. Nordlund, L.M.; Unsworth, R.K.; Wallner-Hahn, S.; Ratnarajah, L.; Beca-Carretero, P.; Boikova, E.; Bull, J.C.; Chefaoui, R.M.; Santos, C.B.d.l.; Gagnon, K.; et al. One hundred priority questions for advancing seagrass conservation in europe. *Plants People Planet* **2024**, *6*, 587–603. [CrossRef]